Missing or Underrated Super-emitters of Nitrogen Oxides in China Exposed from Space

Yuqing Pan[1], Lei Duan[1], Mingqi Li[1], Pinqing Song[1], Nan Xv[1], Jing Liu[1], Shaozhuo Li[1], Yifei Le[2], Cui Wang[2*], Jingjun Ma[1], Xin Zhou[1], Wei Wang[1], Yali Shi[1], Wei Su[1], Gang Wang[1], Liqiang Wang[3], Xue Chen[3], Yan Xia[3], Linhui Jiang[3], Yibo Zhang[3], Mengying Li[3], Zhen Li[3], Weiping Liu[3], Shaocai Yu[3,5*], Daniel Rosenfeld[4], John H. Seinfeld[5], Pengfei Li[1*]

[1]College of Science and Technology, Hebei Agricultural University, Baoding, Hebei 071000, P.R. China
[2]College of Life Science, Zhejiang Chinese Medical University, Hangzhou 310053, Zhejiang, P.R. China
[3]Research Center for Air Pollution and Health; Key Laboratory of Environmental Remediation and Ecological Health, Ministry of Education, College of Environment and Resource Sciences, Zhejiang University, Hangzhou, Zhejiang 310058, P.R. China
[4]Institute of Earth Science, The Hebrew University of Jerusalem, Jerusalem, Israel
[5]Division of Chemistry and Chemical Engineering, California Institute of Technology, Pasadena, CA 91125, USA

[*]Correspondence to: Pengfei Li (lpf_zju@163.com);
Cui Wang (wangcui198506@163.com);
Shaocai Yu (shaocaiyu@zju.edu.cn).

The AMF calculation

The AMF approach was used to convert SCDs to VCDs, which was calculated as following[1–3]:

$$\mathrm{AMF} = \frac{\int_{hs}^{ht} pAMF \times pVCD dh}{\int_{hs}^{ht} pVCD dh} \text{ (Eq. S1).}$$

Therein $\boldsymbol{pVCD}$ represented the partial column of the corresponding layer of the a priori profile, which was obtained from the WRF-CMAQ model. $\boldsymbol{ht}$ and $\boldsymbol{hs}$ denoted the altitude of surface and the tropopause, respectively. For each pixel, $\boldsymbol{pAMF}$ was interpolated from a precalculated look-up table (LUT) derived from the radiative transfer model (RTM) (LIDORT v3.6). The LUT provided the AMFs (i.e., the sensitivity of SCD to VCD in individual atmospheric layers) that were determined by surface reflectance (Rs), surface pressure (Ps), pressure and temperature profiles, aerosol characteristics, cloud fraction (CF), cloud pressure (CP), and NO_2 vertical profile.

For surface reflectance, our method accounted for the effect of the surface bidirectional reflectance distribution function (BRDF). We adopted the MCD43C2 dataset that provided the coefficients for three kernels (isotropic, volumetric, and geometric) and determined the BRDF at 440 nm. Such coefficients were averaged for every 8 days on a 0.5° × 0.5° grid. To fill the missing values, we interpolated the data spatiotemporally using the adjacent two datasets and the surrounding 5 × 5 grid cells. We conducted spatial smoothing on the coefficients to remove the influences from ice or snow, which may not have been fully eliminated in MCD43C2. As a final step, we derived the kernel coefficients for a TROPOMI pixel in a given day from the high-resolution dataset using the spatial mapping and temporal interpolation. This work explicitly accounted for the effect of aerosol optics by including in the RTM calculation the vertical profiles of aerosol extinction coefficient (EC), single scattering albedo (SSA), and phase functions. We adopted the temporally and spatially varying aerosol information (EC, SSA, phase functions, and vertical profiles for individual aerosol types) at the local time of TROPOMI pixels from the WRF-CMAQ simulation. The surface albedo, surface pressure, cloud fraction, cloud albedo, and cloud pressure were obtained from the TROPOMI cloud product.

Background correction

In this study, background values were subtracted from the tropospheric NO_2 VCDs. For each pixel, the specific background value was set as the 5th percentile of the corresponding VCDs. Without such a background correction, the NO_x sinks (including chemical, deposition, horizontal, and diffusional loss) would be systematically biased high in our top-down model. This was because that the assumed lifetime (i.e., 4 hours) was appropriate for anthropogenic pollution in lower tropospheric background[4] rather than the upper troposphere.

NO_2/NO_x ratio

The tropospheric NO_2 VCDs were scaled to NO_x by $\boldsymbol{r}$. The partitioning of NO_x into NO and NO_2 depended on atmospheric chemical reactions involving ozone concentrations, temperature, and actinic fluxes. As numerous previous studies, we assumed a scaling factor of $\boldsymbol{r}$ =0.76[6,7]. This condition corresponded to cloud-free conditions around noon and general air pollution.

However, this assumption might differ, particularly when O_3 is titrated in a fresh plume. In this case, however, the fresh emitted NO would not be visible from satellite measurements. Once NO is converted to NO_2 via O_3, the satellite-based NO_2 VCDs would be enhanced in the downwind area of the super-emitter. For the quantification of total NO_x emissions, the NO_x/NO_2 ratio after reaching equilibrium would still be appropriate.

Steady state

We assumed steady states by ignoring changes in the wind patterns and emissions. In a single daily VCD map, NO_x plumes were a result of emission accumulations and variable winds. Such plumes caused dipole-like patterns in the divergence, as the calculated flux increased at one edge of the plume and decreased by the same amount at the other edge. As these dipole patterns varied from day to day, these dipole-like patterns were mostly canceled out. Such effects can be investigated using upcoming geostationary satellite instruments (GEMS[8], TEMPO[9], Sentinel-4[10]) that can track the plumes hourly.

Previous studies have demonstrated that the steady state was generally a reasonable assumption for fresh plumes, and the potential error due to the abovementioned nonstationary state would become acceptable when approaching a point source. Thus, the identified super-emitters would not be affected by the steady state assumption.

Uncertainty analysis

This work lays a foundation for rethinking the localized NO_x budget and guiding the emission mitigation. The reliability of the identifications and quantifications for NO_x super-emitters was supported by comparisons to the satellite imageries and to a state-of-the-art bottom-up inventory. However, more extensive validations (e.g., continuous emission monitoring systems for industrial parks) were needed for a better mechanistic understanding of NO_x sources and sinks and reducing uncertainties of our approach presented here.

As explained in Methods, the uncertainty in the assumed NO_x lifetime represented the main uncertainty. In theory, the general NO_x lifetime would be consistent with the measured and predicted information in the literature (Table S1). Given the fine-scale sizes of the grids and the typical horizontal wind speeds, the lifetime should likely be closer to a few hours for the super-emitters. The resulting emission fluxes were likely larger than those estimated using a longer lifetime. To provide robust identifications and quantifications, we calculated the NO_x emission fluxes using conservative lower and upper bounds on the lifetime of 1 and 24 hours. As a result, the super-emitters would still be recognized since the adjustment of the lifetime setting would not largely subvert the emission gradients on a fine-scale (Fig. S10). On the other hand, the corresponding results were shown as error bars in Fig. 3, keeping following our above findings.

Besides, the vertical profile for retrieving the satellite-based NO_x VCDs in this study was obtained from the WRF-CMAQ model simulations driven by MEICv1.3 for the year 2016. In theory, the bottom-up emission inventory plays a key role in spatiotemporal distributions of air pollution[11,12]. To what extent uncertainties on the vertical profile could introduce biases, we analyzed our satellite-based NO_x VCDs derived from the MEICv1.2-driven (the base year was 2012) WRF-CMAQ model simulations. Here we calculated the differences between these two kinds of VCDs for the entire year. As shown in the histogram (Fig. S11), differences were of the order of 1 ± 17%. These statistics were representative for the entire nation, but locally errors for the super-emitters can be larger. It should also be stressed that this analysis depended on the similarity between these two vertical profiles, which may be different from the actual vertical profiles.

Reference

1. Su, W. *et al.* An improved TROPOMI tropospheric HCHO retrieval over China. *Atmos. Meas. Tech. Discuss.* **2020**, 1–26 (2020).
2. Liu, M. *et al.* A new TROPOMI product for tropospheric NO_2 columns over East Asia with explicit aerosol corrections. *Atmos. Meas. Tech.* **13**, 4247–4259 (2020).
3. Lin, J.-T. *et al.* Retrieving tropospheric nitrogen dioxide from the Ozone Monitoring Instrument: effects of aerosols, surface reflectance anisotropy, and vertical profile of nitrogen dioxide. *Atmos. Chem. Phys.* **14**, 1441–1461 (2014).
4. Beirle, S., Boersma, K. F., Platt, U., Lawrence, M. G. & Wagner, T. Megacity emissions and lifetimes of nitrogen oxides probed from space. *Scienc.* **333**, 1737–1739 (2011).
5. Silvern, R. F. *et al.* Using satellite observations of tropospheric NO_2 columns to infer long-term trends in US NO_x emissions: the importance of accounting for the free tropospheric NO_2 background. *Atmos. Chem. Phys.* **19**, 8863–8878 (2019).
6. Seinfeld, J. H. Urban Air Pollution: State of the Science. *Science.* **243**, 745–752 (1989).
7. Beirle, S. *et al.* Pinpointing nitrogen oxide emissions from space. *Sci. Adv.* **5**, eaax9800 (2019).
8. Kim, J. *et al.* New Era of Air Quality Monitoring from Space: Geostationary Environment Monitoring Spectrometer (GEMS). *Bull. Am. Meteorol. Soc.* **101**, E1–E22.
9. Chance, K. *et al.* TEMPO Green Paper: Chemistry, physics, and meteorology experiments with the Tropospheric Emissions: monitoring of pollution instrument. in *Proc.SPIE* vol. 11151 (2019).
10. Ingmann, P. *et al.* Requirements for the GMES Atmosphere Service and ESA's implementation concept: Sentinels-4/-5 and-5p. *Remote Sens. Environ.* **120**, 58–69 (2012).
11. Li, M. *et al.* MIX: a mosaic Asian anthropogenic emission inventory under the international collaboration framework of the MICS-Asia and HTAP. *Atmos. Chem. Phys.* **17**, (2017).
12. Zhang, Q. *et al.* Drivers of improved $PM_{2.5}$ air quality in China from 2013 to 2017. *Proc. Natl. Acad. Sci.* (2019).
13. Liu, F. *et al.* NO_x lifetimes and emissions of cities and power plants in polluted background estimated by satellite observations. *Atmos. Chem. Phys.* **16**, 5283 (2016).

14. Kong, H. *et al.* High-resolution (0.05*0.05) NO_x emissions in the Yangtze River Delta inferred from OMI. *Atmos. Chem. Phys.* **19**, 12835–12856 (2019).

15. Laughner, J. L. & Cohen, R. C. Direct observation of changing NO_x lifetime in North American cities. *Science.* **366**, 723–727 (2019).

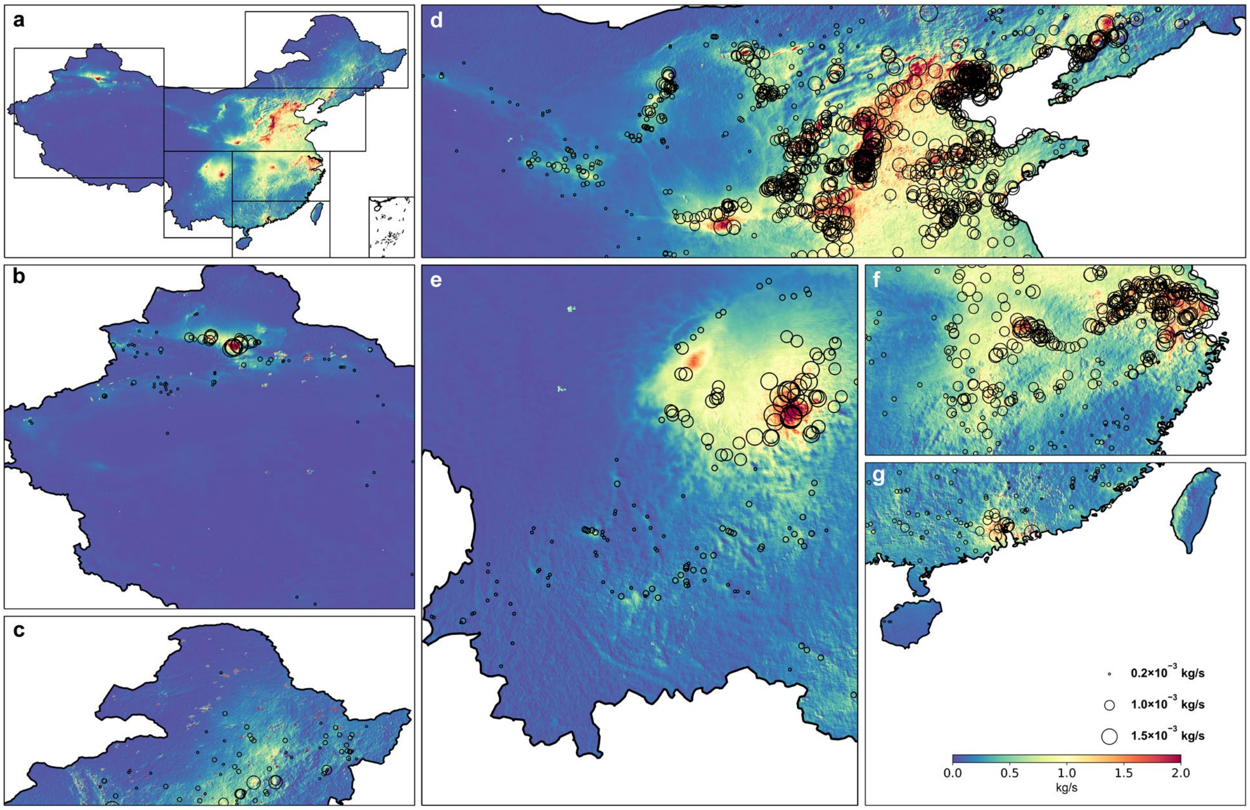

Fig. S1. One-year averages of NO_x emissions based on the TROPOMI instrument. a, One-year averages of NO_x emissions across China. **b ~ g**, Zoom-ins over Northwest, Northeast, North, Southwest, East, and South China.

146

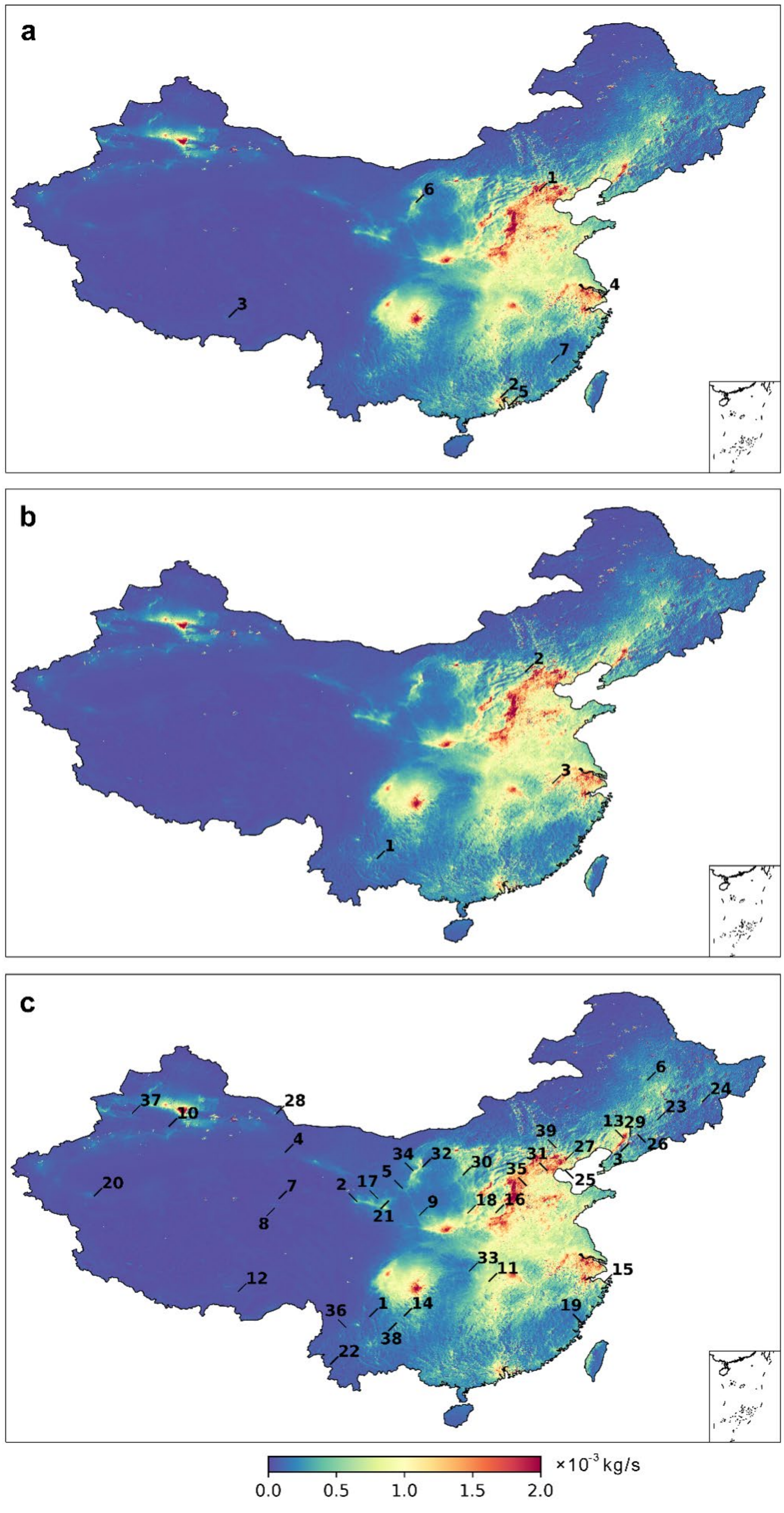

a
1
6
4
3
7
2
5
b
2
3
1
c
6
24
37
28
23
10
13
29
26
4
39
27
34
32
30
31
3
5
35
25
20
2
17
7
21
9
18
16
8
33
11
15
12
36
1
14
19
38
22
×10⁻³ kg/s
0.0
0.5
1.0
1.5
2.0

Fig. S2. Locations of the (a) cities, (b) rural areas, and (c) super-emitters discussed in the main text on top of one-year oversampled NO_x VCDs. The cities, rural areas, and super-emitters are sorted by the initials. The cities include (1) Beijing, (2) Guangzhou, (3) Lhasa, (4) Shanghai, (5) Shenzhen, (6) Shizuishan, and (7) Yongan. The rural areas include (1) Chetian, (2) Jiqingbao, and (3) Pangjing. The super-emitters include (1) Baihetan, (2) Baitong, (3) Beiying, (4) Chengbei, (5) Daguohe, (6) Daqing, (7) Geermu, (8) Guolemude, (9) Hailuo, (10) Hejing, (11) Huagang, (12) Huaxin, (13) Hunhe, (14) Jiangtian, (15) Jiaochuan, (16) Jincheng, (17) Lanxing, (18) Longmen, (19) Longzhudou, (20) Luopu, (21) Maligou, (22) Mengsheng, (23) Mingcheng, (24) Mudanjiang, (25) Nanbao, (26) Nanzamu, (27) Peijiafen, (28) Rundajianeng, (29) Sanbaotun, (30) Shengbang, (31) Shidian, (32) Shizuishan, (33) Tanjiazui, (34) Tianhua, (35) Xincheng, (36) Yongbao, (37) Zeketai, (38) Zhongjing, and (39) Zhongluan. The detailed information is shown in Supplementary Table 2.

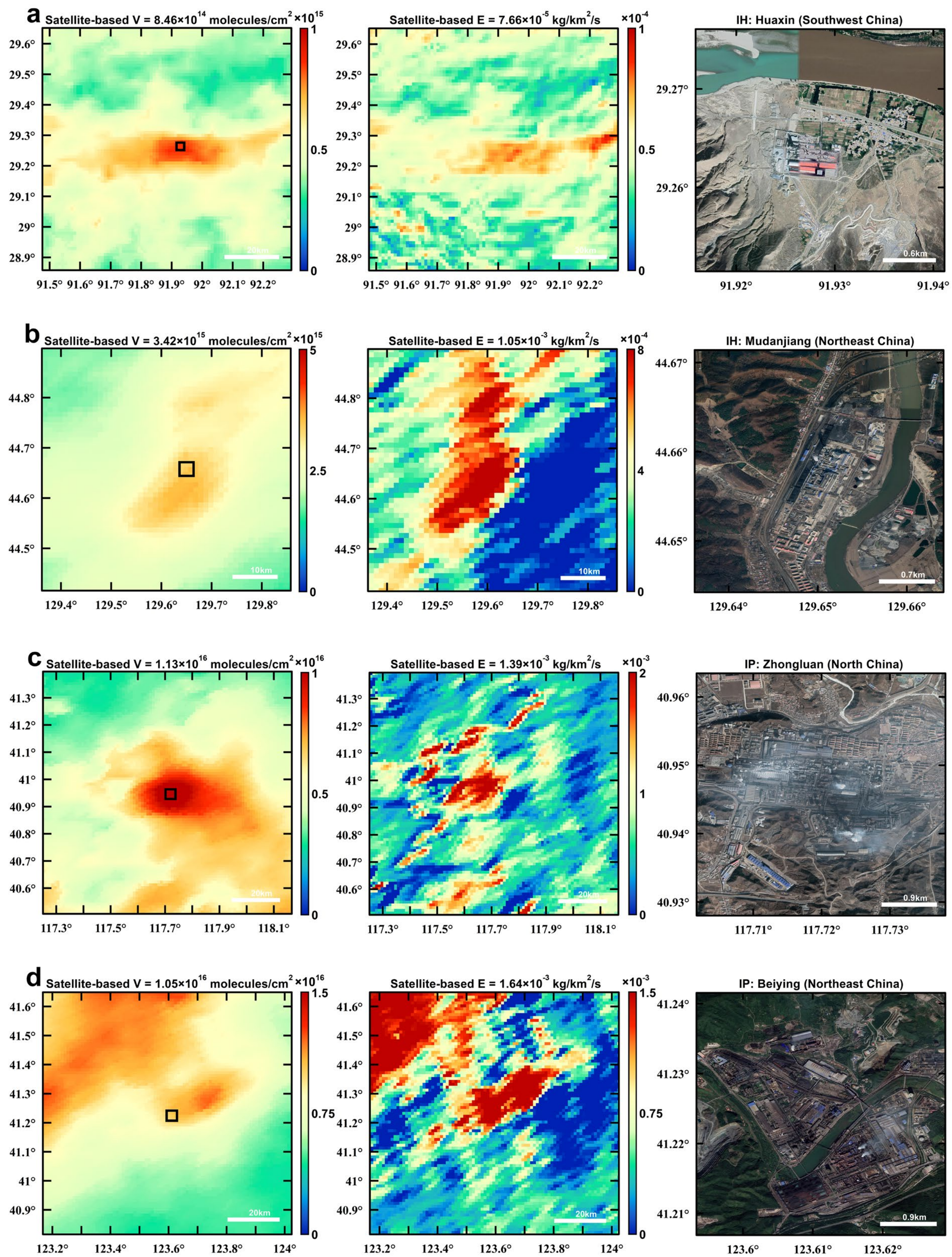

Fig. S3. The same as Fig. 2 but for different super-emitters (Fig. S3a ~ S3d).

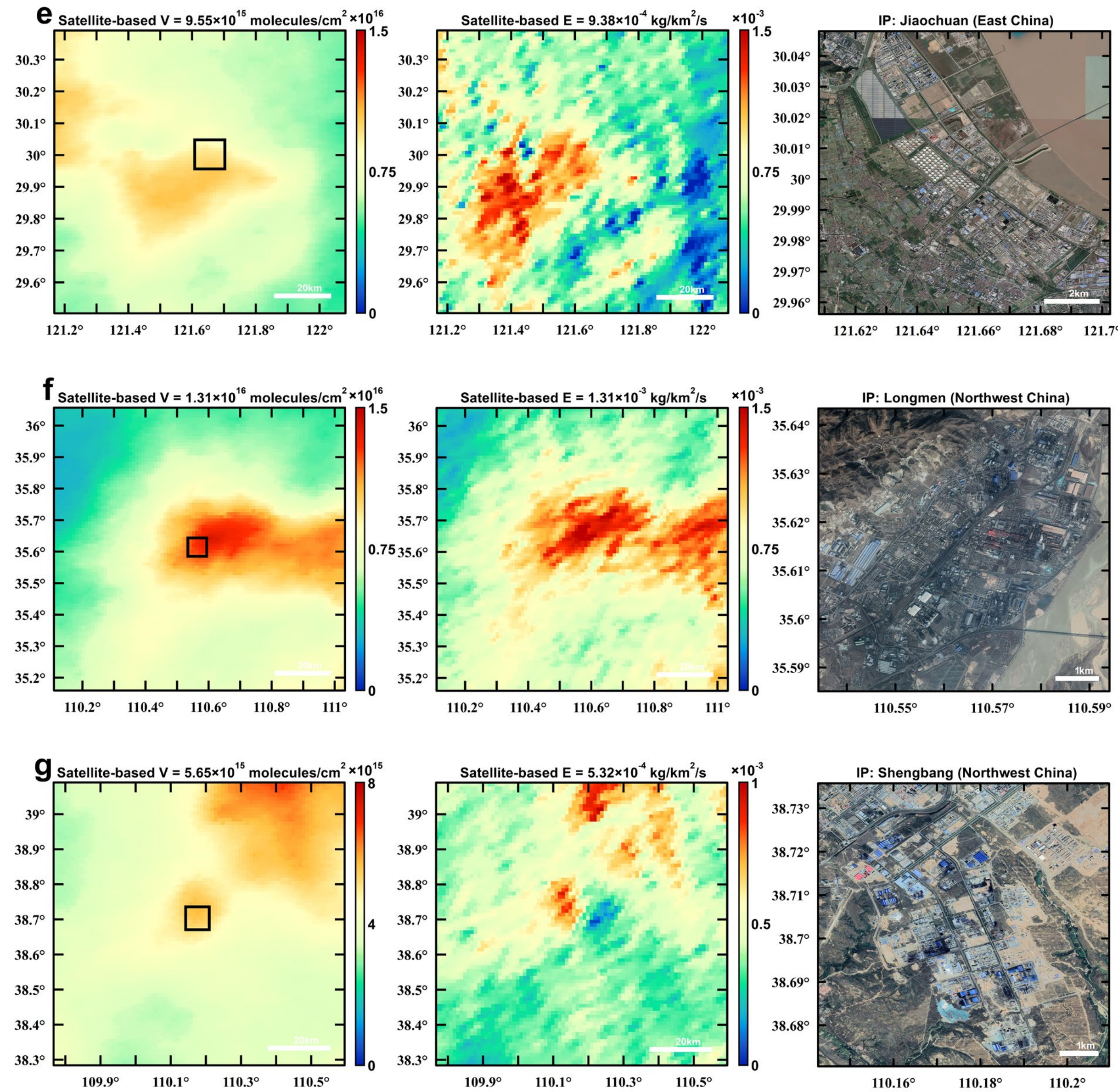

Fig. S3. The same as Fig. 2 but for different super-emitters (Fig. S3e ~ S3g).

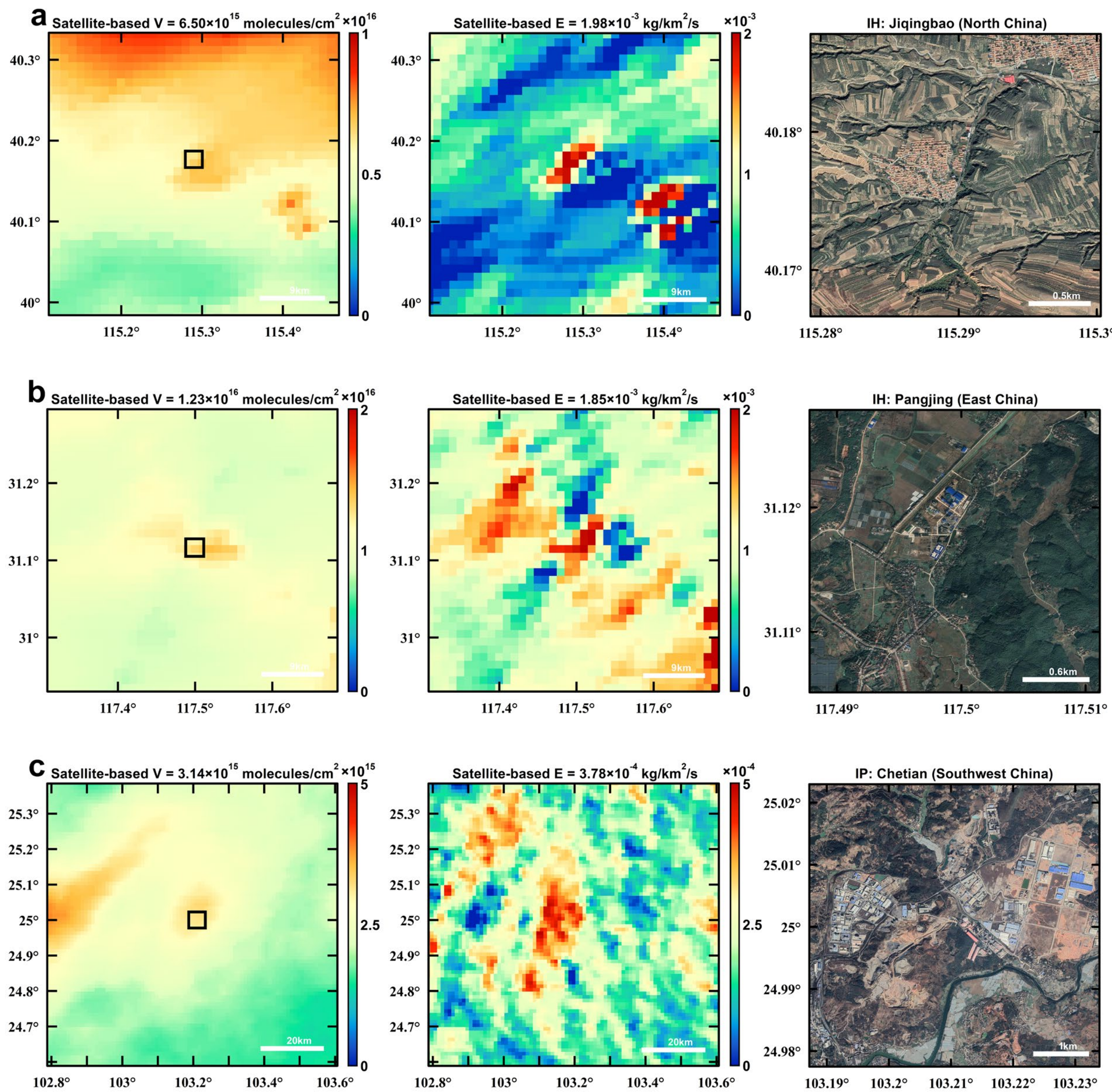

Fig. S4. The same as Fig. 2 but for rural areas and cities (Fig. S4a ~ S4c).

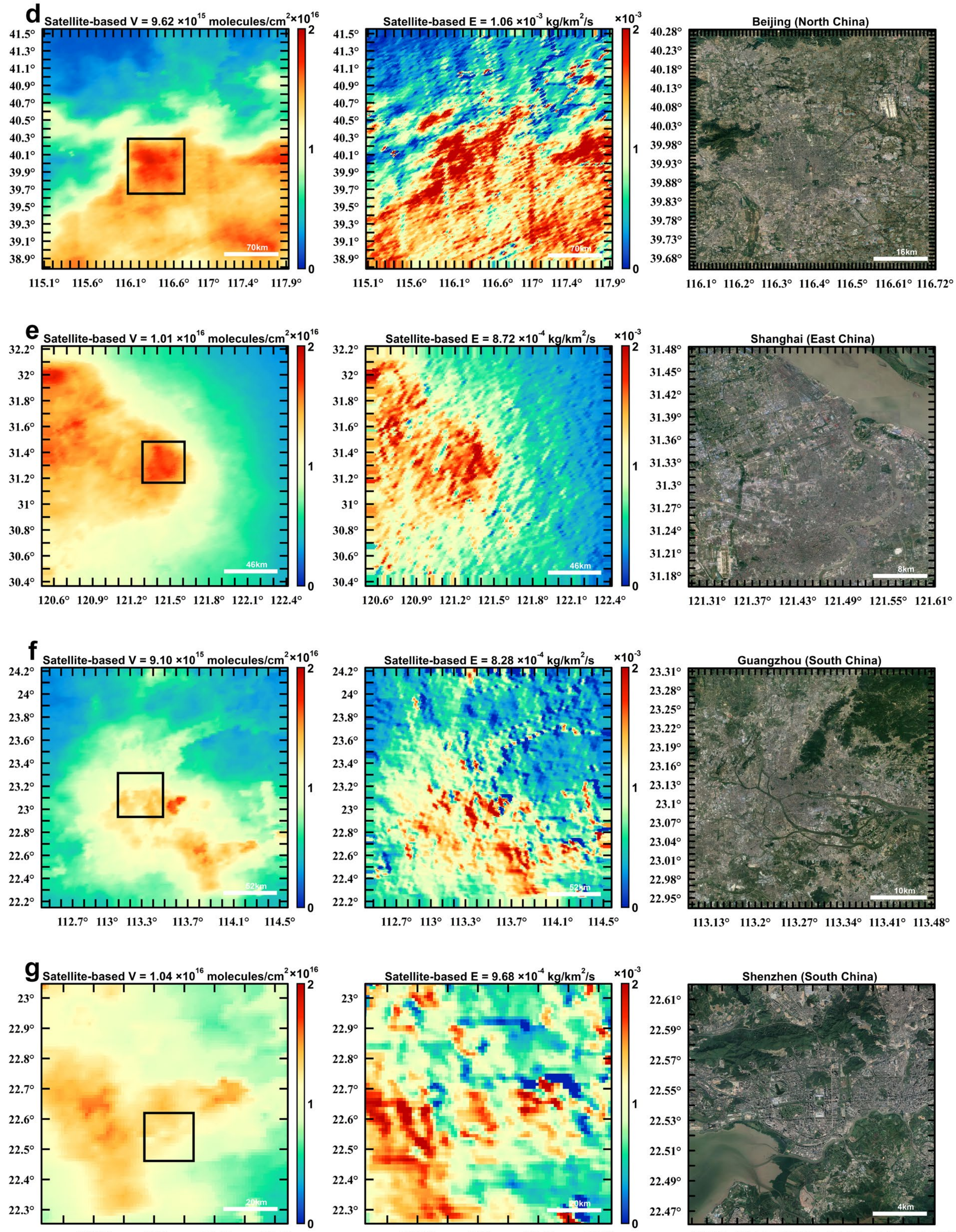

Fig. S4. The same as Fig. 2 but for rural areas and cities (Fig. S4d ~ S4g).

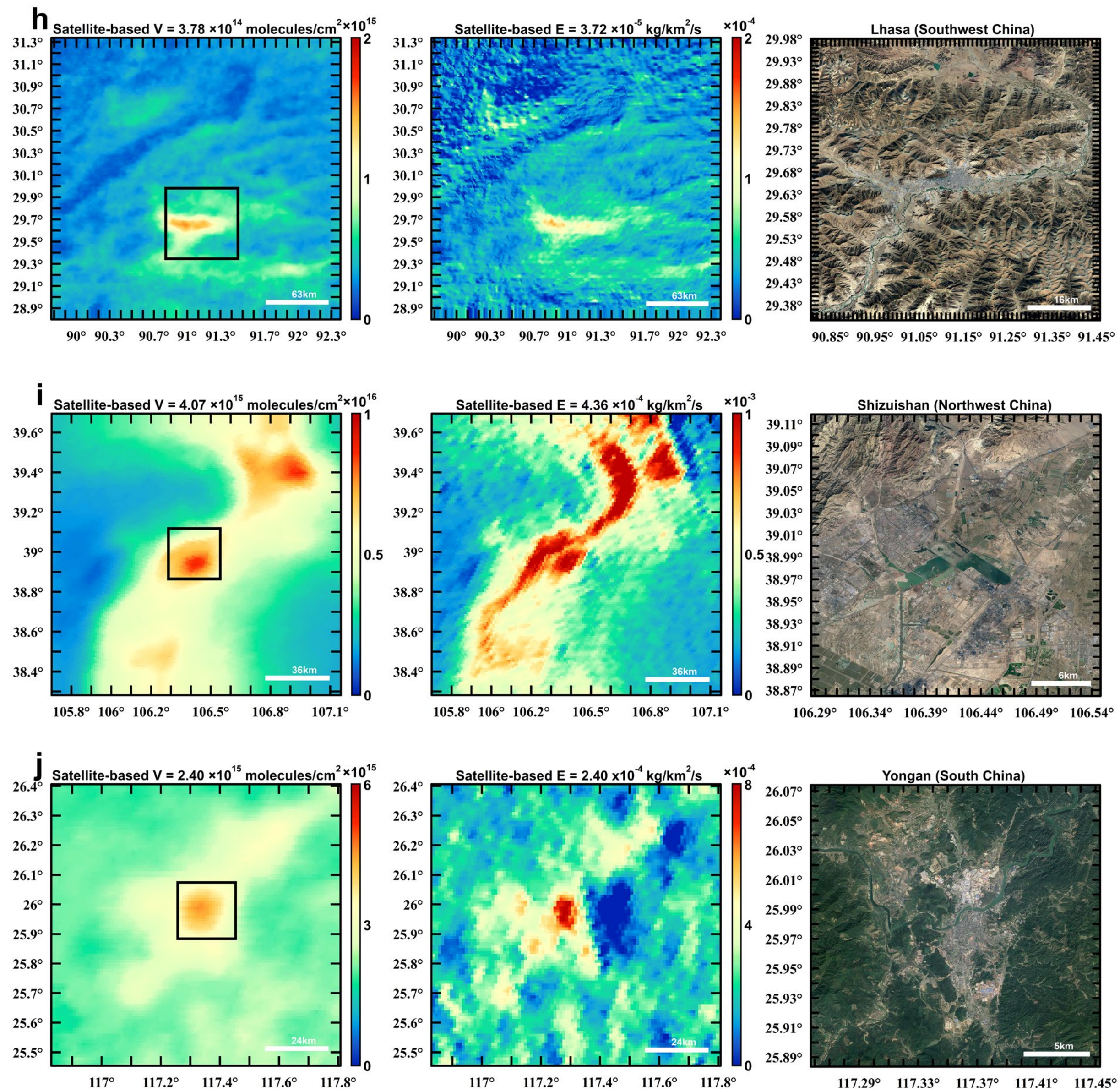

Fig. S4. The same as Fig. 2 but for rural areas and cities (Fig. S4h ~ S4j).

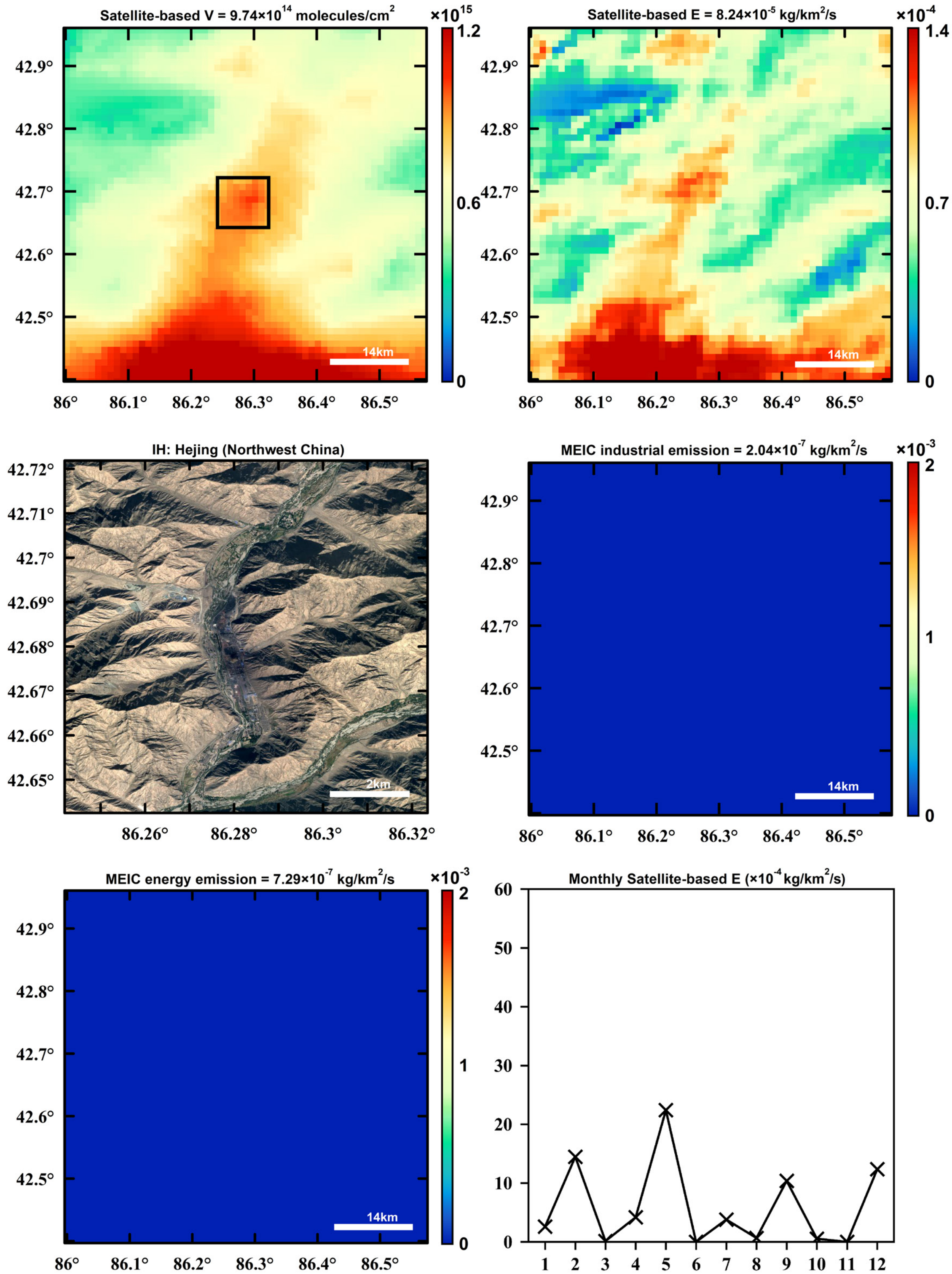

Fig. S5. The same as Fig. 2 but for different super-emitters. Besides, for each super-emitter, the emission fluxes from the industry and power plant sectors in MEICv1.3 and the monthly variations in the satellite-based emission fluxes are also presented **(Fig. S5a)**. MEICv1.3 directly missed this super-emitter.

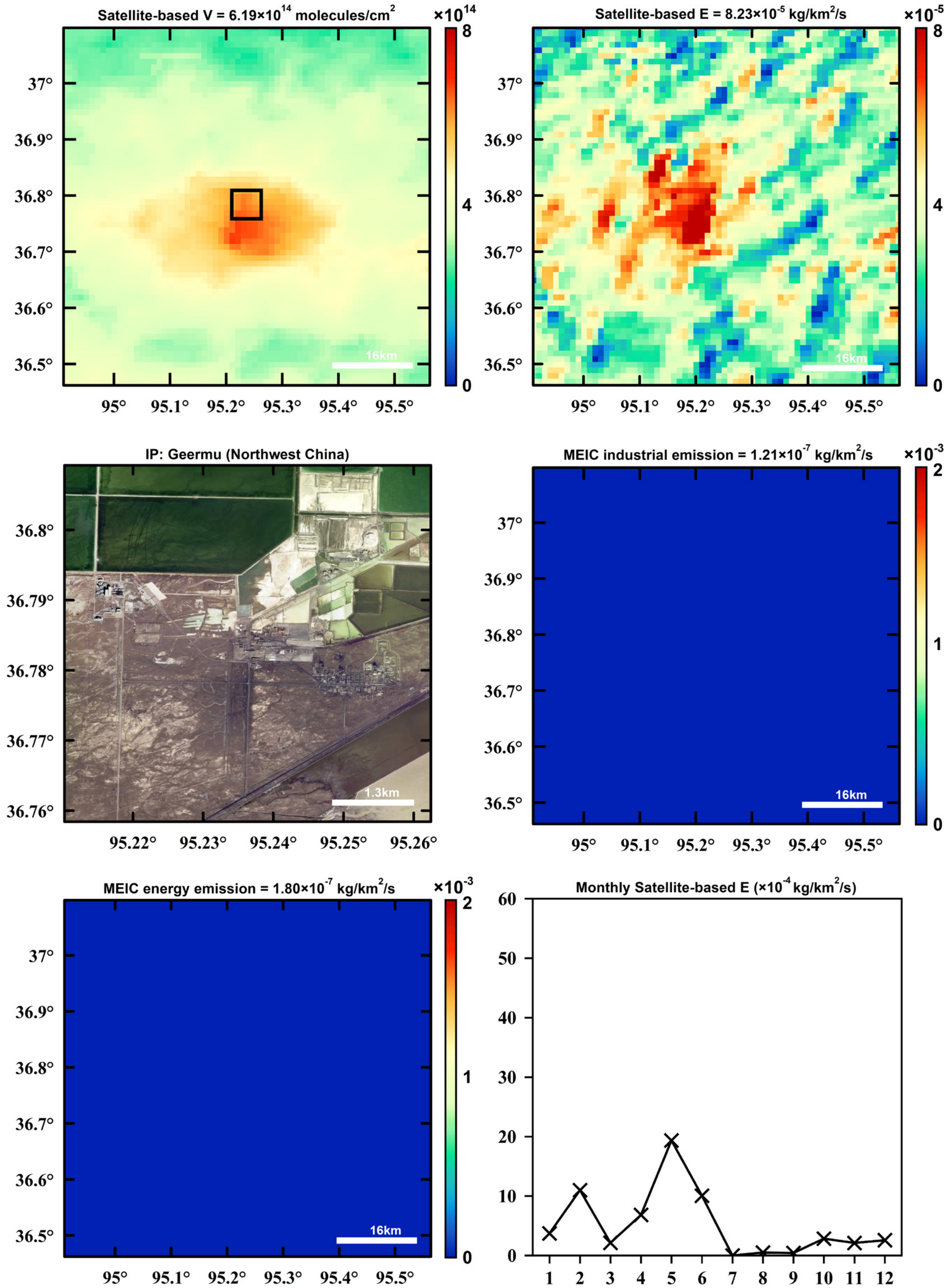

Fig. S5. The same as Fig. 2 but for different super-emitters. Besides, for each super-emitter, the emission fluxes from the industry and power plant sectors in MEICv1.3 and the monthly variations in the satellite-based emission fluxes are also presented **(Fig. S5b)**. MEICv1.3 directly missed this super-emitter.

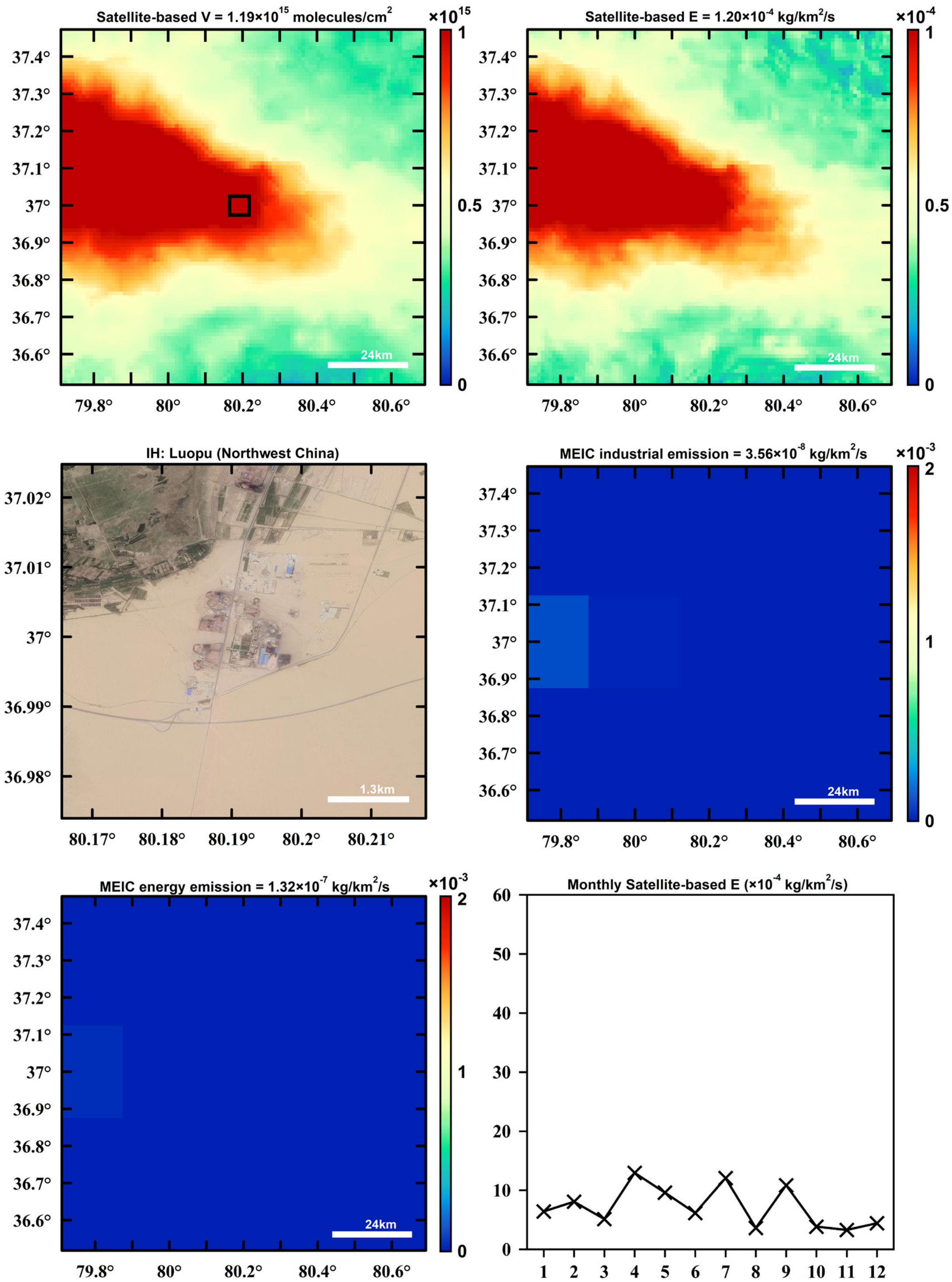

Fig. S5. The same as Fig. 2 but for different super-emitters. Besides, for each super-emitter, the emission fluxes from the industry and power plant sectors in MEICv1.3 and the monthly variations in the satellite-based emission fluxes are also presented **(Fig. S5c)**. MEICv1.3 directly missed this super-emitter.

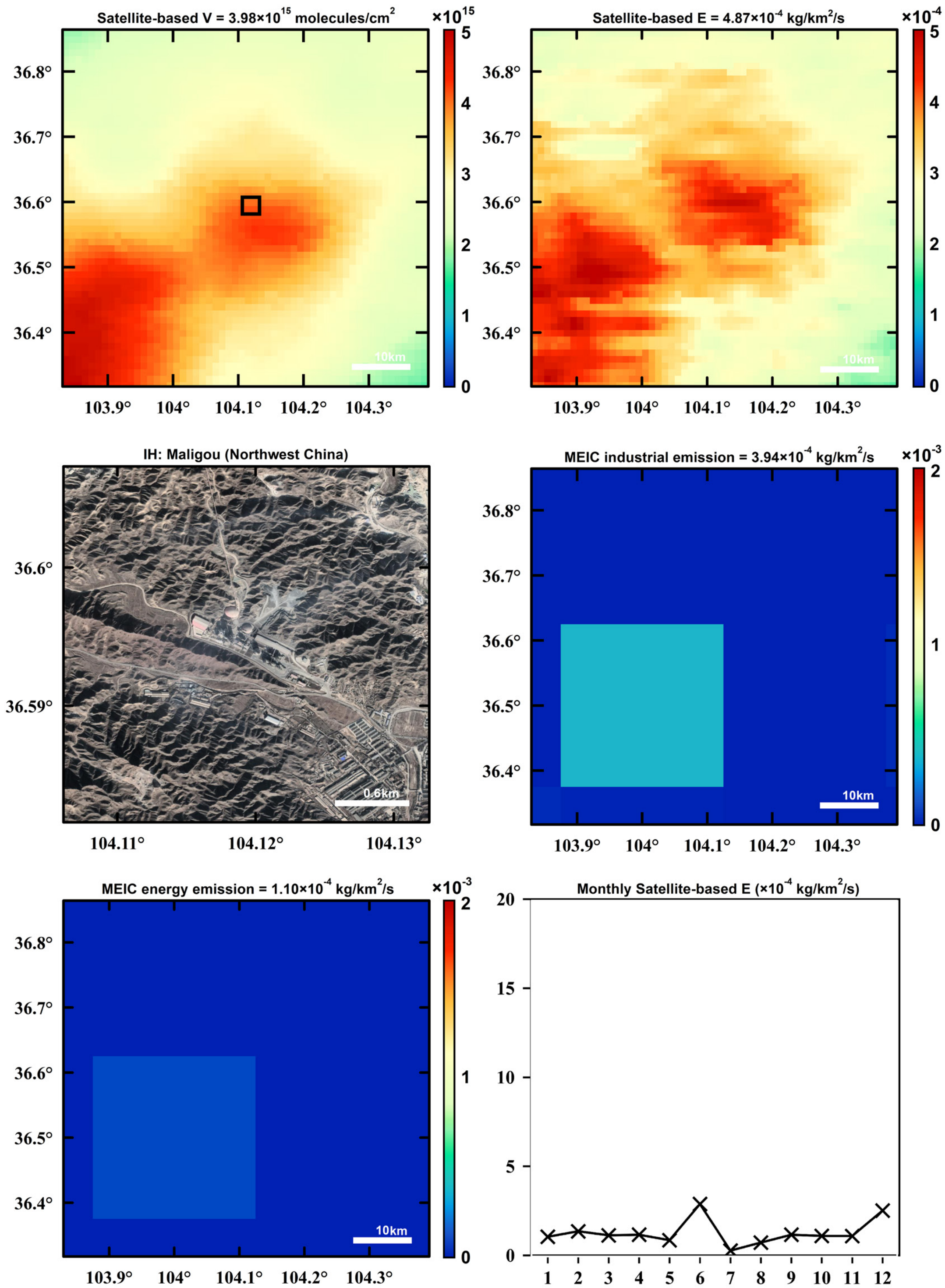

Fig. S5. The same as Fig. 2 but for different super-emitters. Besides, for each super-emitter, the emission fluxes from the industry and power plant sectors in MEICv1.3 and the monthly variations in the satellite-based emission fluxes are also presented **(Fig. S5d)**.

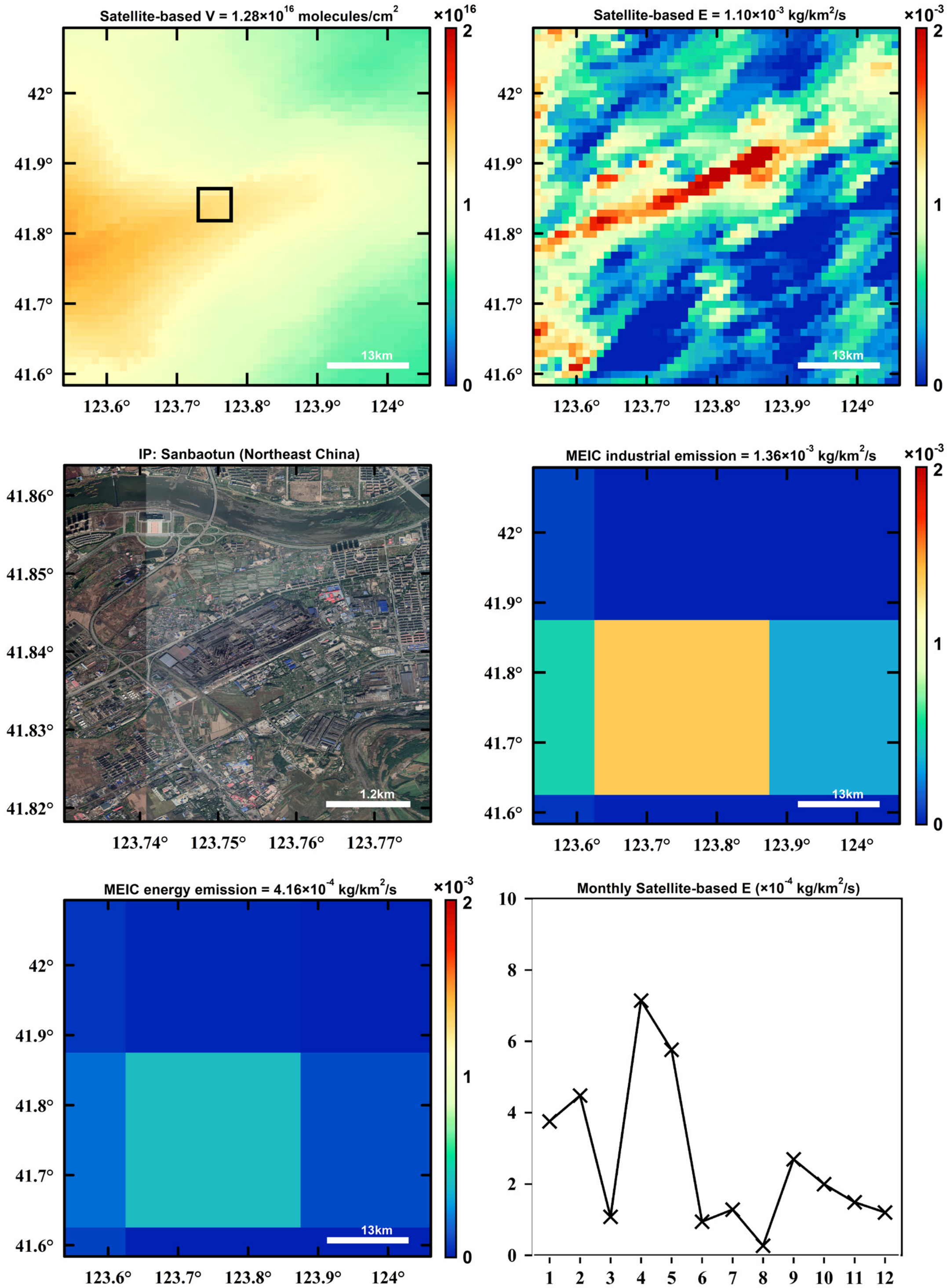

Fig. S5. The same as Fig. 2 but for different super-emitters. Besides, for each super-emitter, the emission fluxes from the industry and power plant sectors in MEICv1.3 and the monthly variations in the satellite-based emission fluxes are also presented **(Fig. S5e)**.

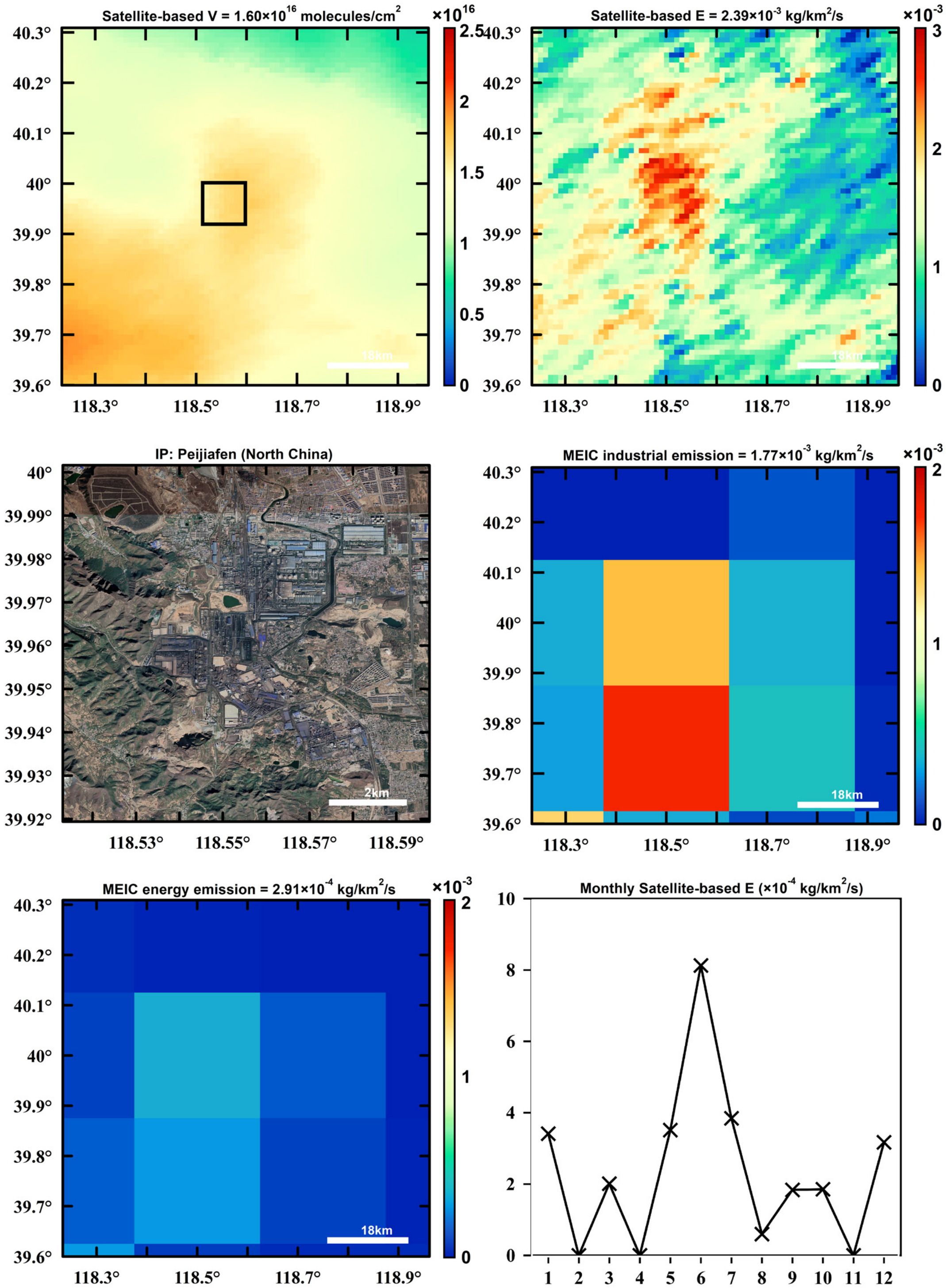

Fig. S5. The same as Fig. 2 but for different super-emitters. Besides, for each super-emitter, the emission fluxes from the industry and power plant sectors in MEICv1.3 and the monthly variations in the satellite-based emission fluxes are also presented **(Fig. S5f)**.

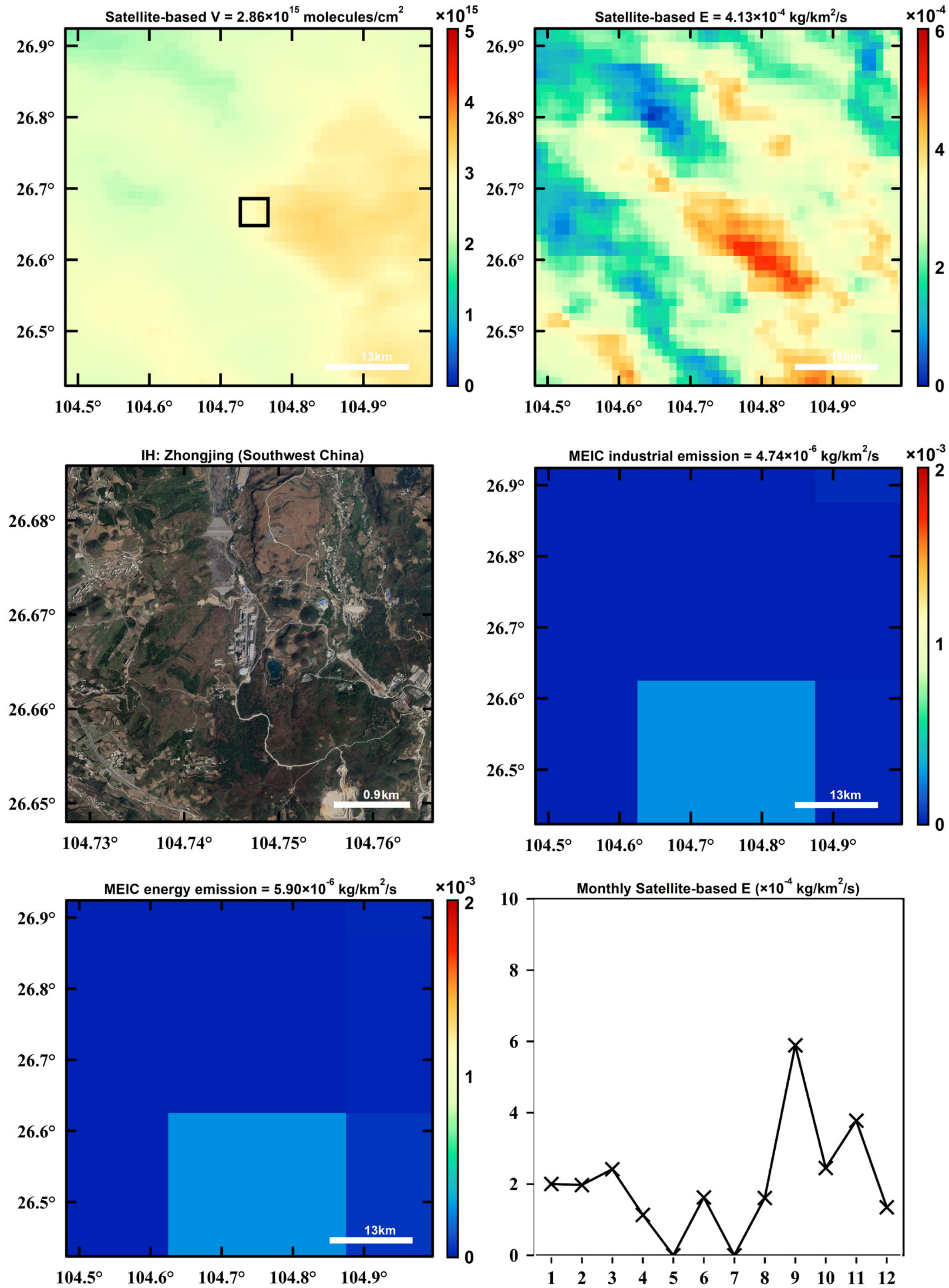

Fig. S5. The same as Fig. 2 but for different super-emitters. Besides, for each super-emitter, the emission fluxes from the industry and power plant sectors in MEICv1.3 and the monthly variations in the satellite-based emission fluxes are also presented **(Fig. S5g)**.

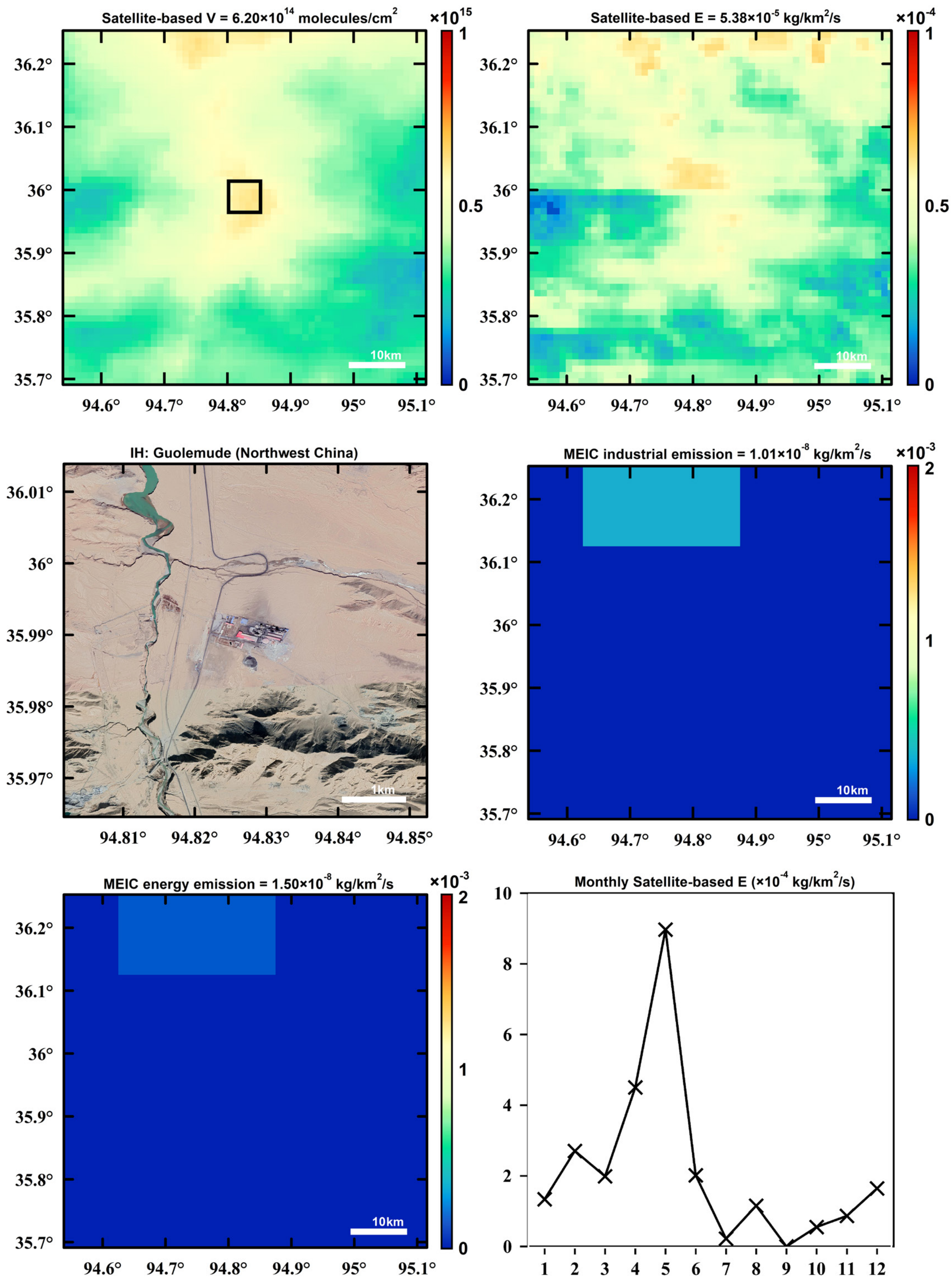

Fig. S5. The same as Fig. 2 but for different super-emitters. Besides, for each super-emitter, the emission fluxes from the industry and power plant sectors in MEICv1.3 and the monthly variations in the satellite-based emission fluxes are also presented **(Fig. S5h)**.

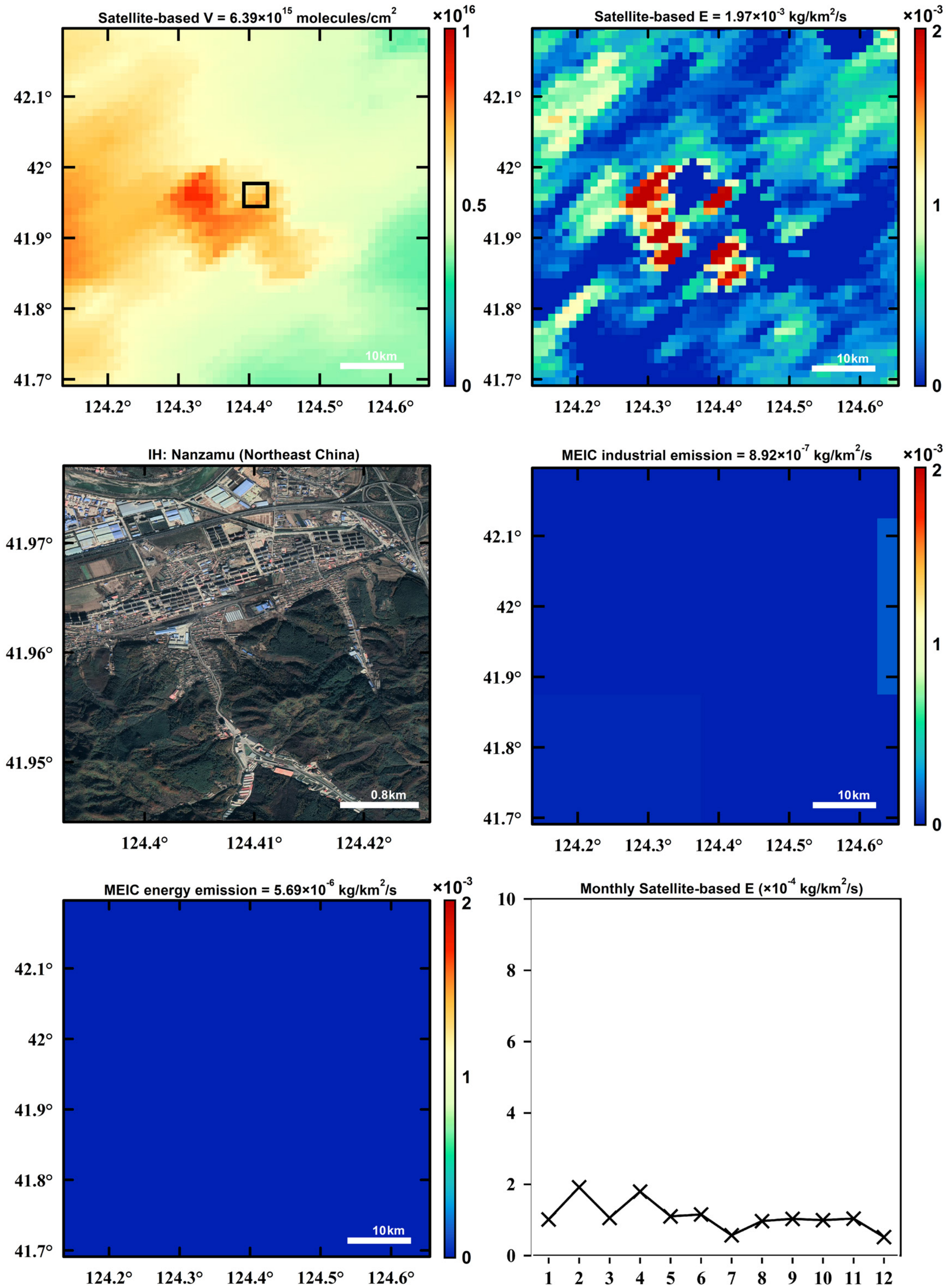

Fig. S5. The same as Fig. 2 but for different super-emitters. Besides, for each super-emitter, the emission fluxes from the industry and power plant sectors in MEICv1.3 and the monthly variations in the satellite-based emission fluxes are also presented **(Fig. S5i)**.

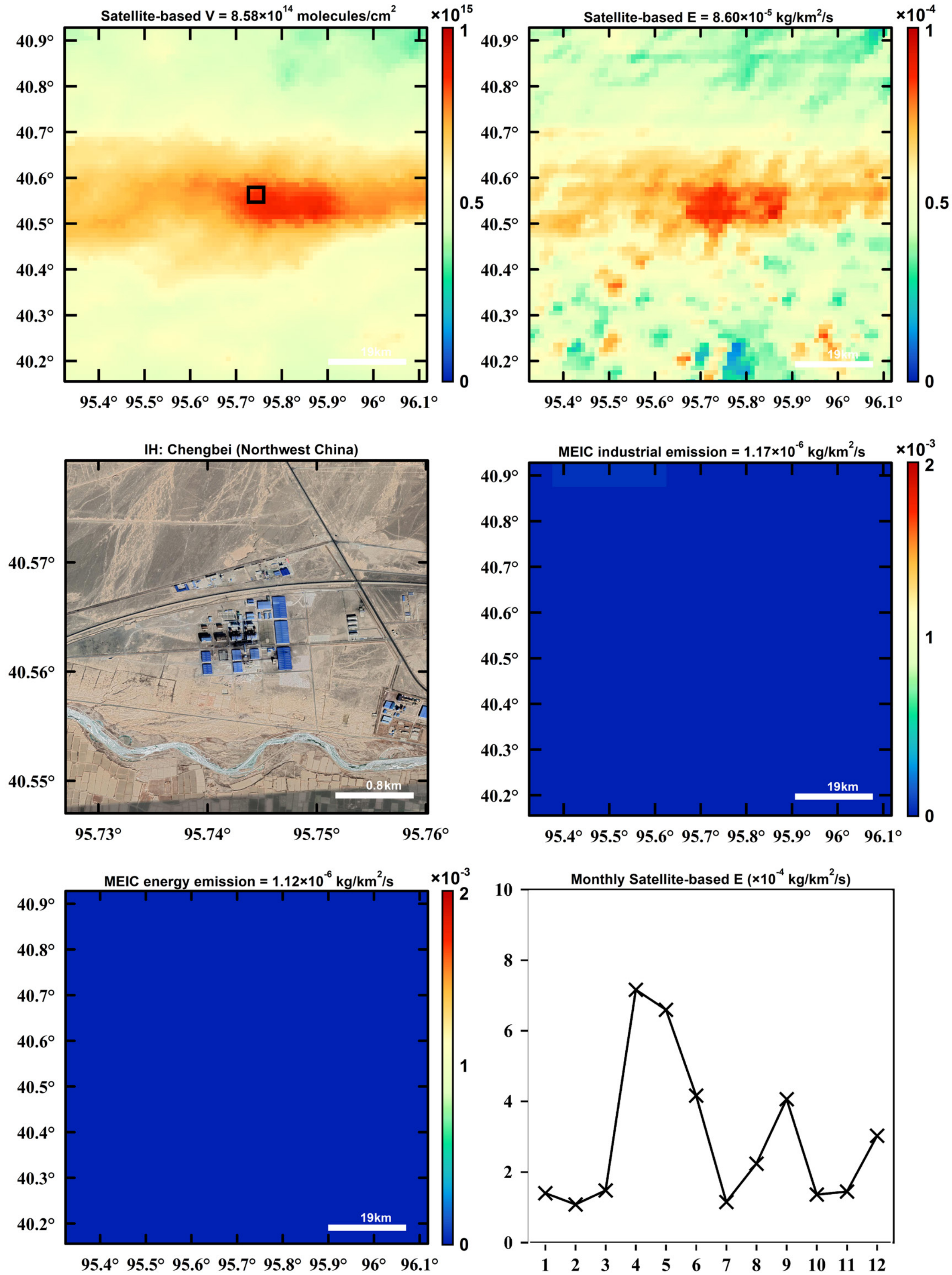

Fig. S5. The same as Fig. 2 but for different super-emitters. Besides, for each super-emitter, the emission fluxes from the industry and power plant sectors in MEICv1.3 and the monthly variations in the satellite-based emission fluxes are also presented **(Fig. S5j)**.

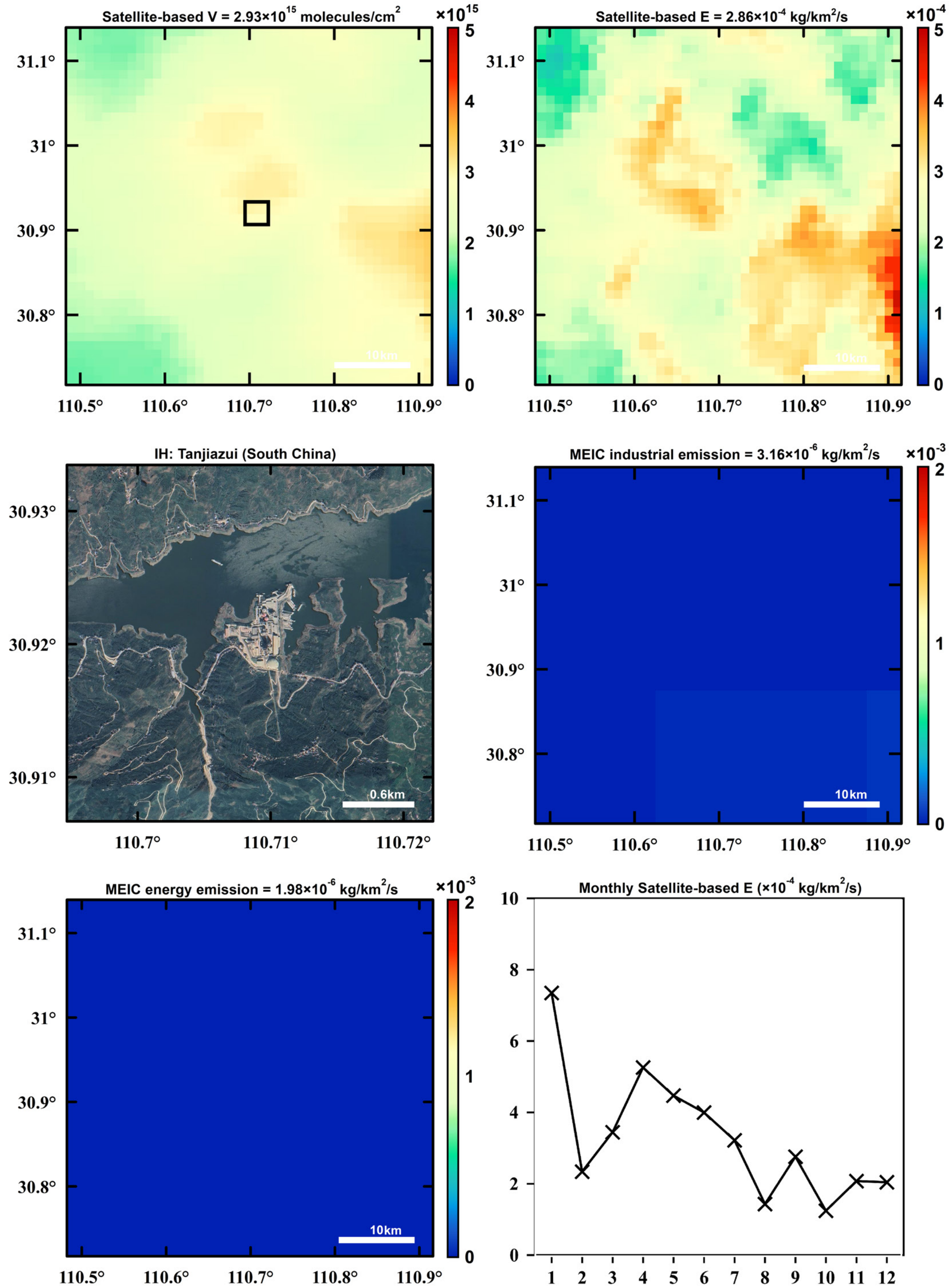

Fig. S5. The same as Fig. 2 but for different super-emitters. Besides, for each super-emitter, the emission fluxes from the industry and power plant sectors in MEICv1.3 and the monthly variations in the satellite-based emission fluxes are also presented **(Fig. S5k)**.

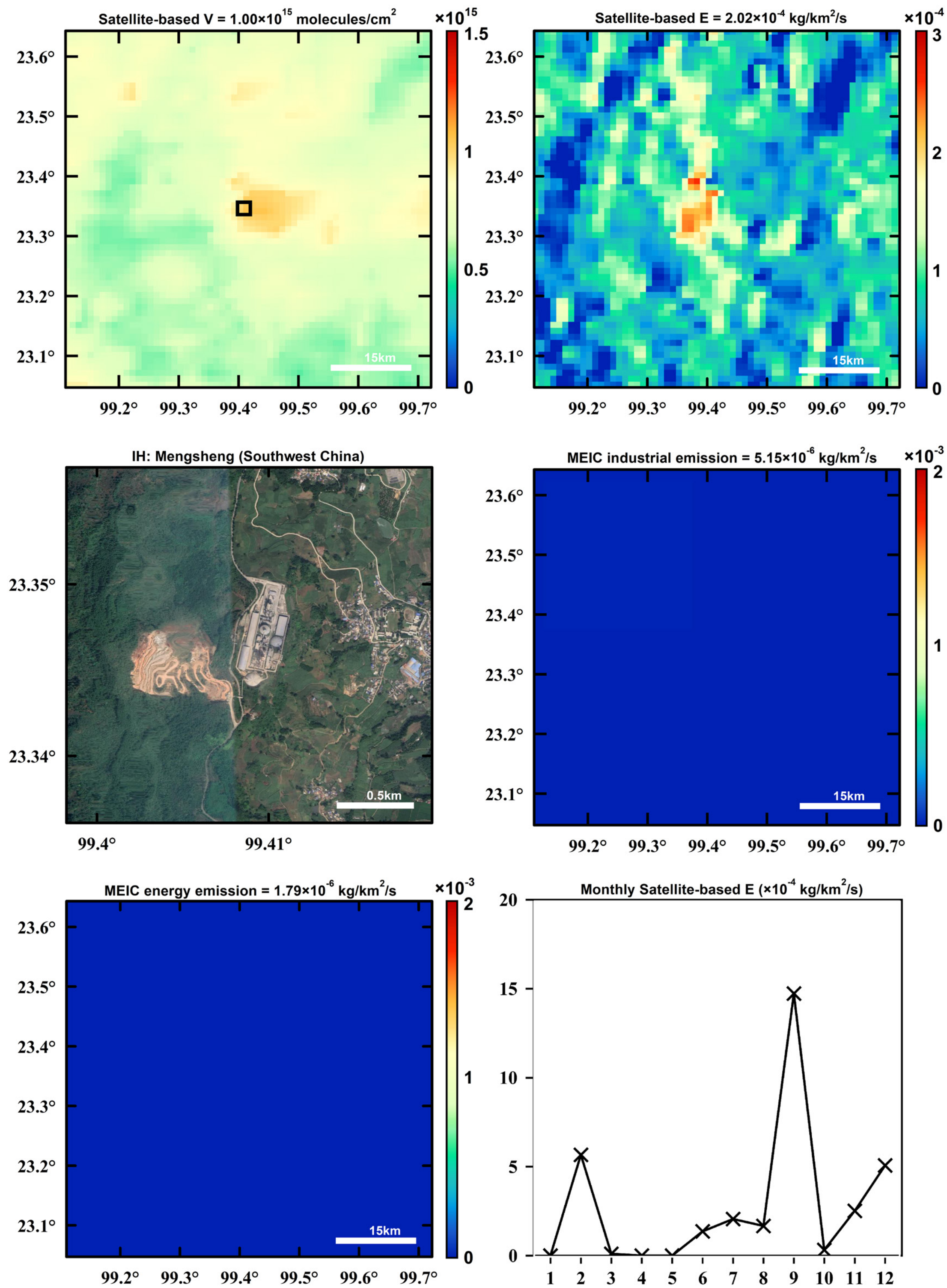

Fig. S5. The same as Fig. 2 but for different super-emitters. Besides, for each super-emitter, the emission fluxes from the industry and power plant sectors in MEICv1.3 and the monthly variations in the satellite-based emission fluxes are also presented **(Fig. S5l)**.

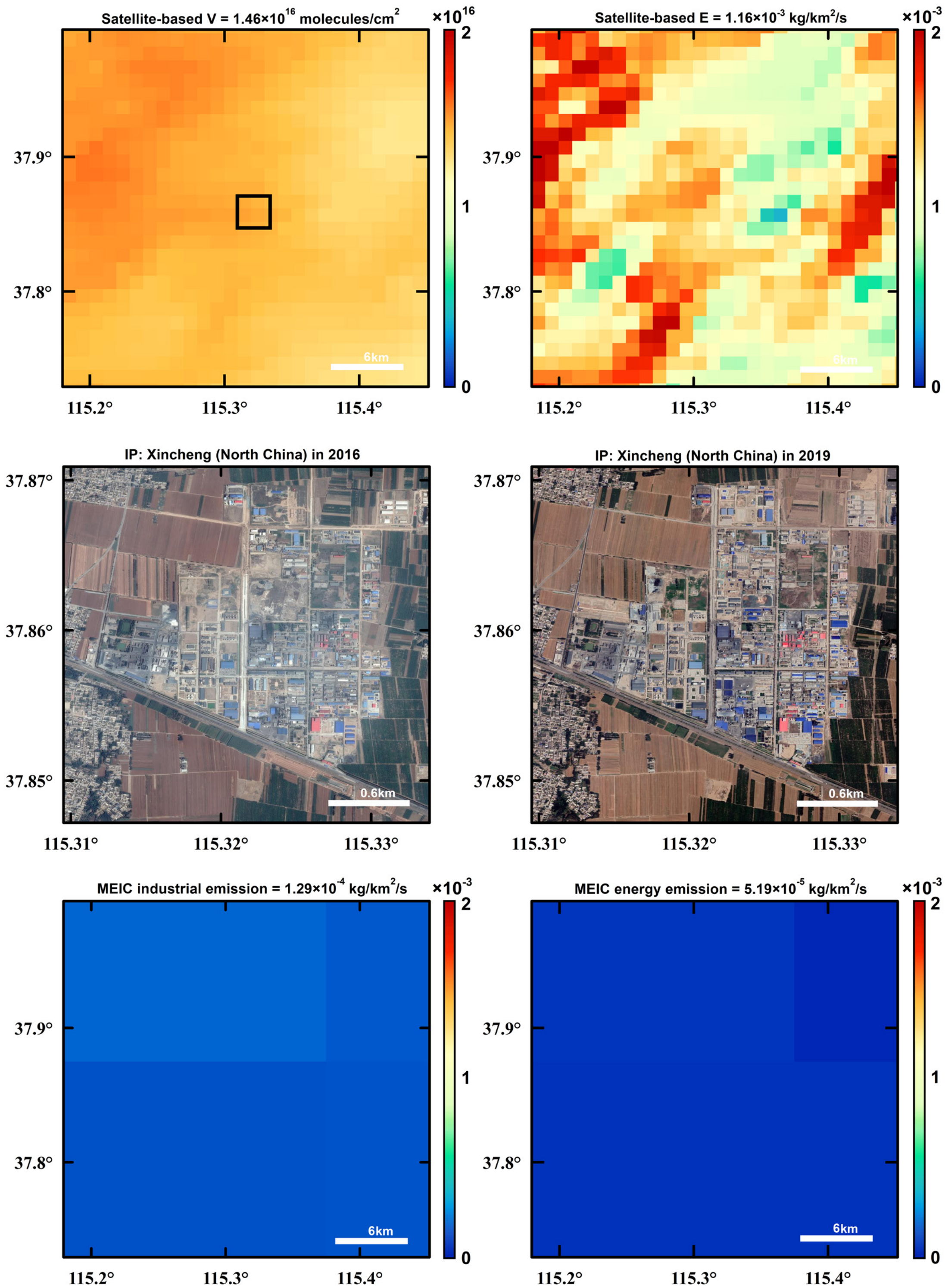

Fig. S6. The onset (a, b) or the discontinuation (c, d) of super-emitters. For each super-emitter, the TROPOMI-based NO_x VCDs and emissions, the satellite images in 2016 and 2019 from the Landsat 8 imageries, and the emission fluxes from the industry and power plant sectors in MEICv1.3 **(Fig. S6a).**

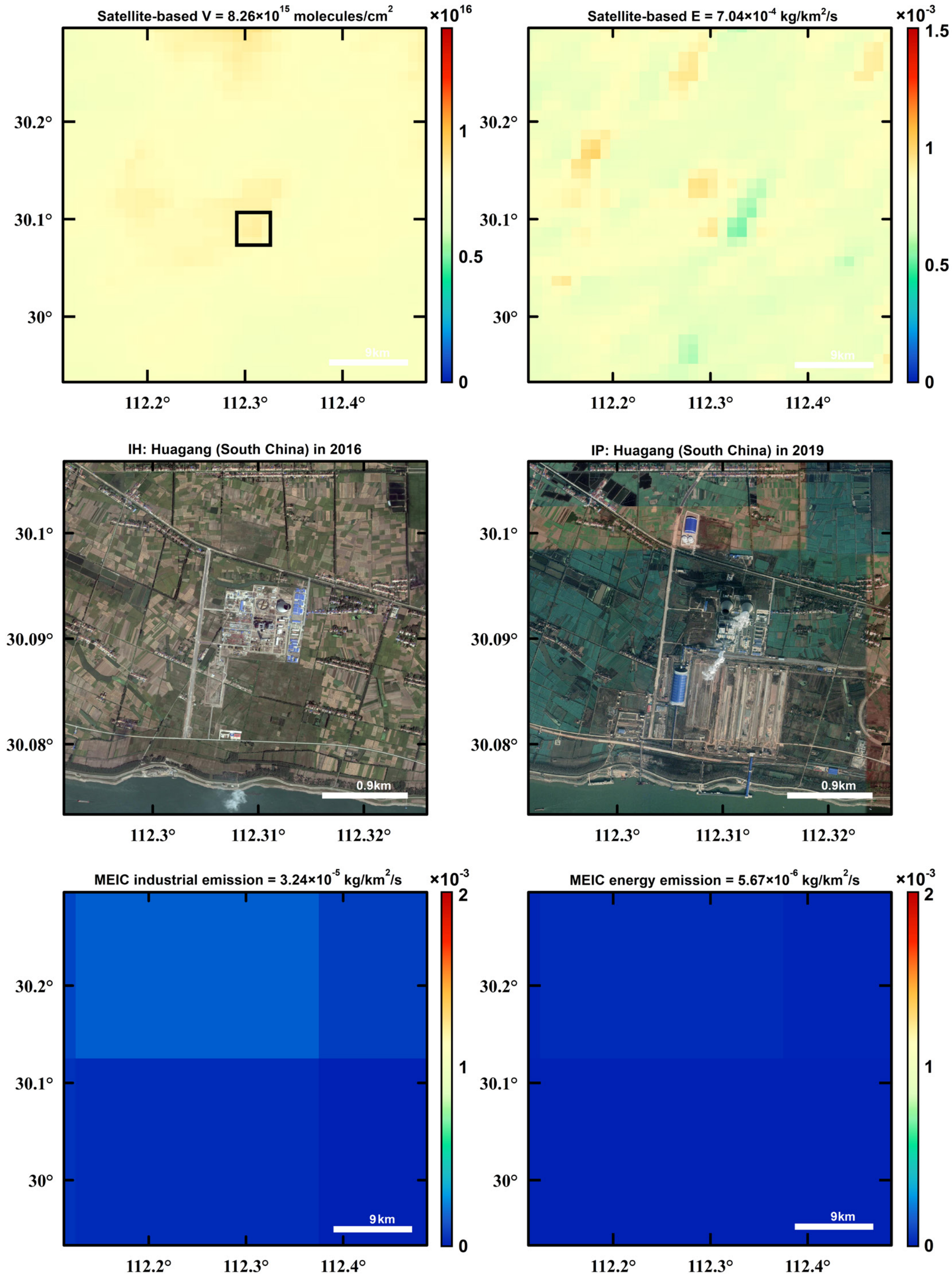

Fig. S6. The onset (a, b) or the discontinuation (c, d) of super-emitters. For each super-emitter, the TROPOMI-based NO_x VCDs and emissions, the satellite images in 2016 and 2019 from the Landsat 8 imageries, and the emission fluxes from the industry and power plant sectors in MEICv1.3 **(Fig. S6b).**

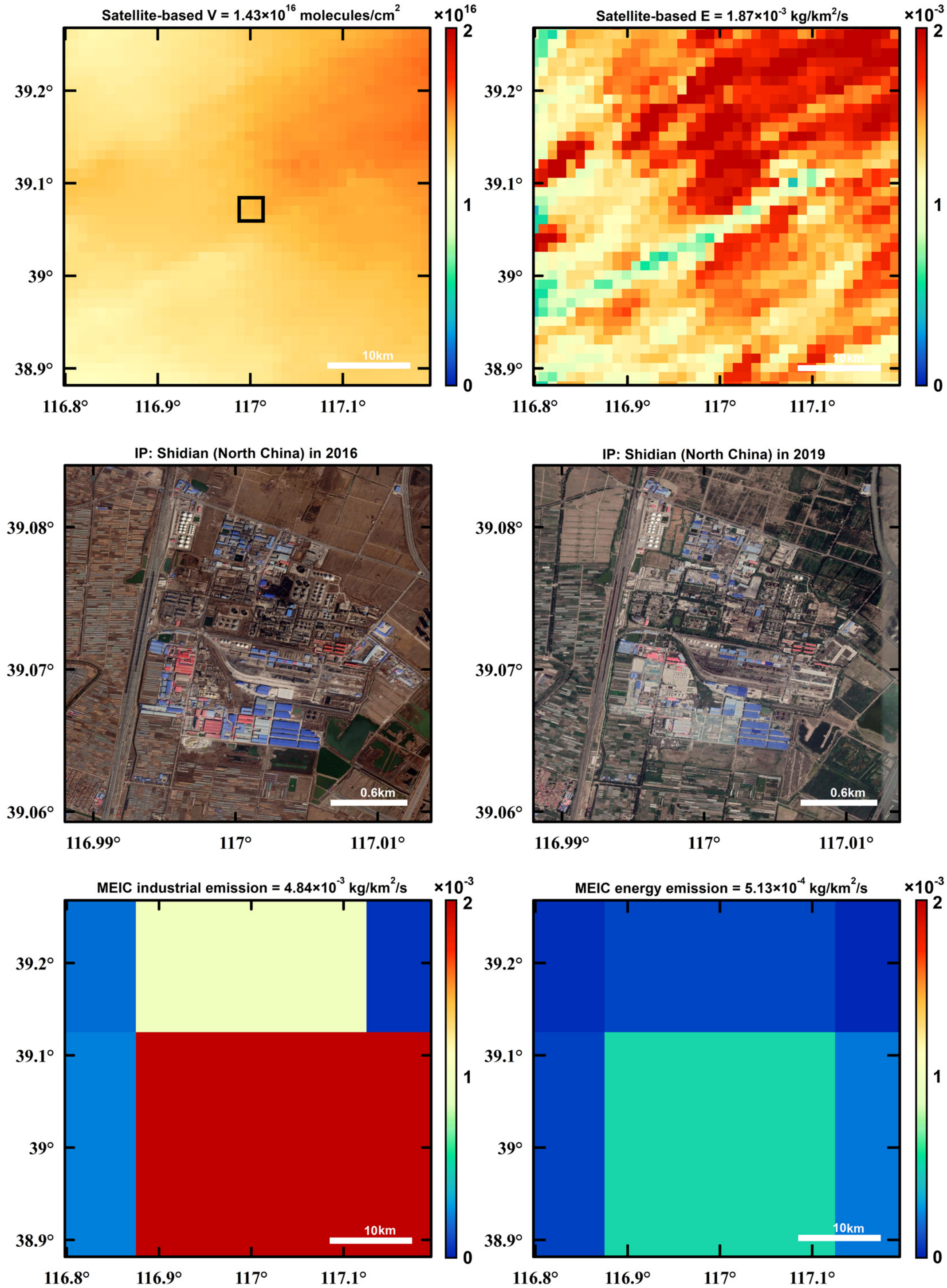

Fig. S6. The onset (a, b) or the discontinuation (c, d) of super-emitters. For each super-emitter, the TROPOMI-based NO_x VCDs and emissions, the satellite images in 2016 and 2019 from the Landsat 8 imageries, and the emission fluxes from the industry and power plant sectors in MEICv1.3 **(Fig. S6c).**

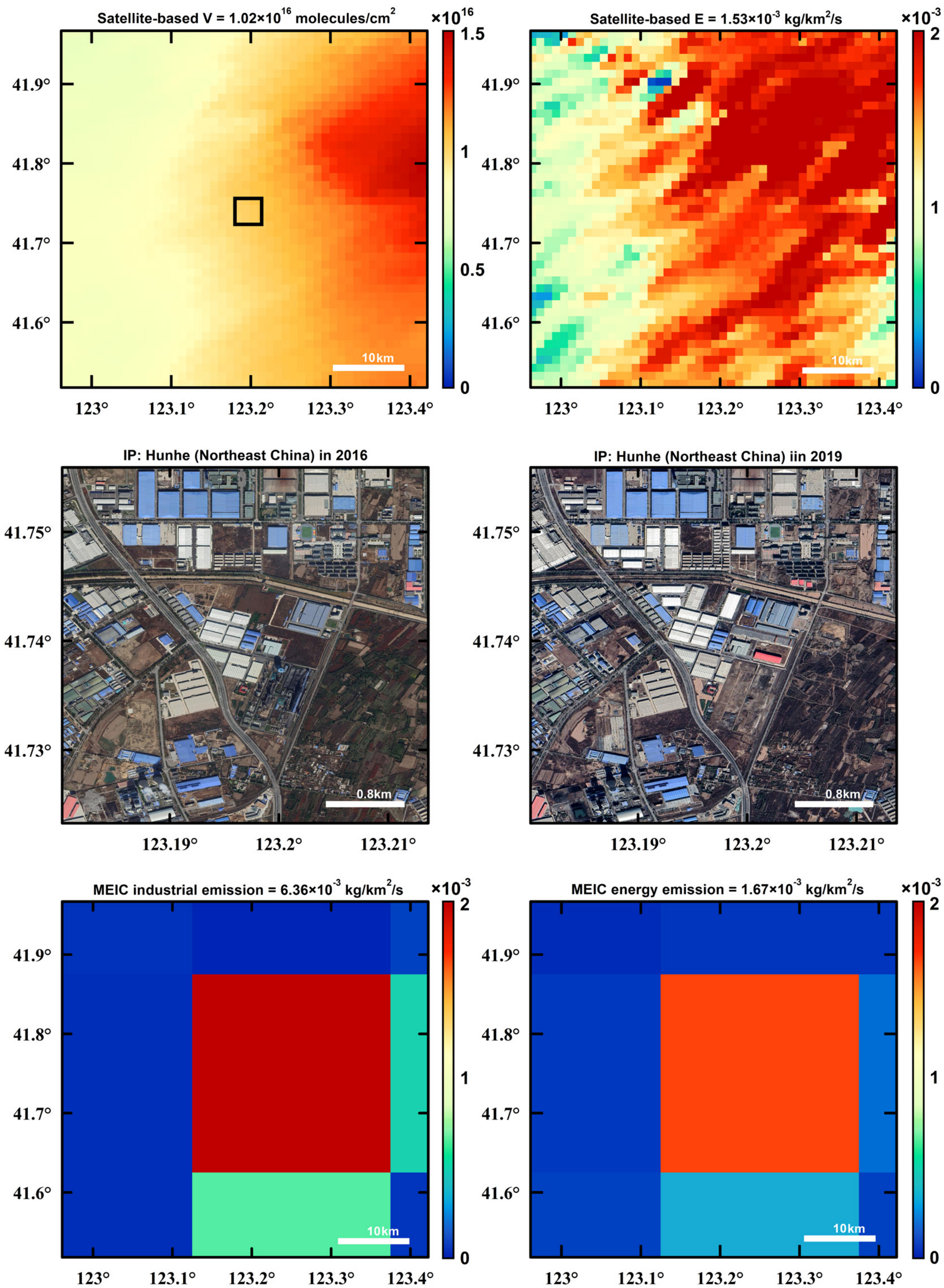

Fig. S6. The onset (a, b) or the discontinuation (c, d) of super-emitters. For each super-emitter, the TROPOMI-based NO_x VCDs and emissions, the satellite images in 2016 and 2019 from the Landsat 8 imageries, and the emission fluxes from the industry and power plant sectors in MEICv1.3 **(Fig. S6d).**

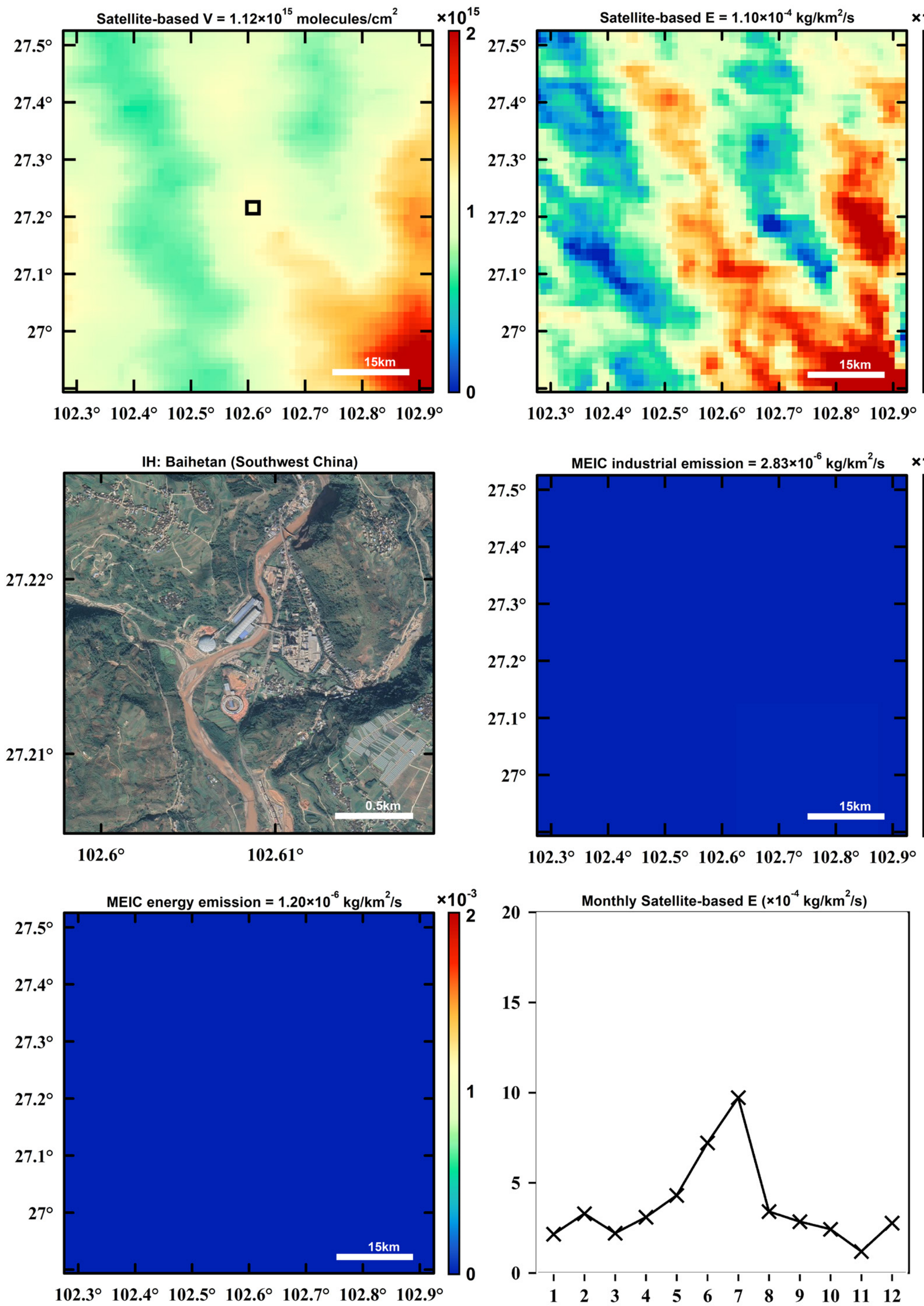

Fig. S7. The same as Fig. 2 but for different super-emitters. The representative super-emitters show stable monthly variations in the satellite-based NO_x emission fluxes **(Fig. S7a)**.

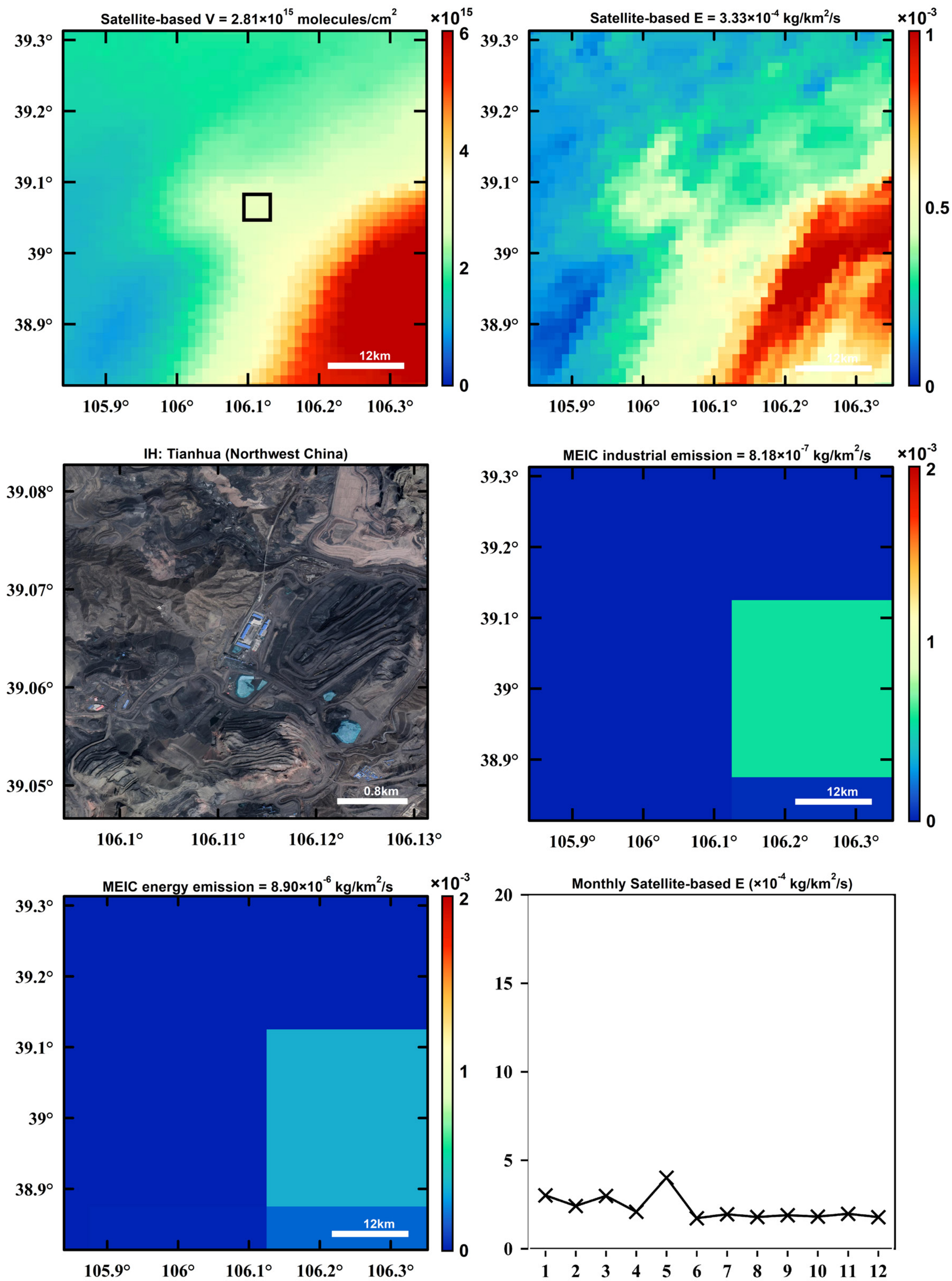

Fig. S7. The same as Fig. 2 but for different super-emitters. The representative super-emitters show stable monthly variations in the satellite-based NO_x emission fluxes **(Fig. S7b)**.

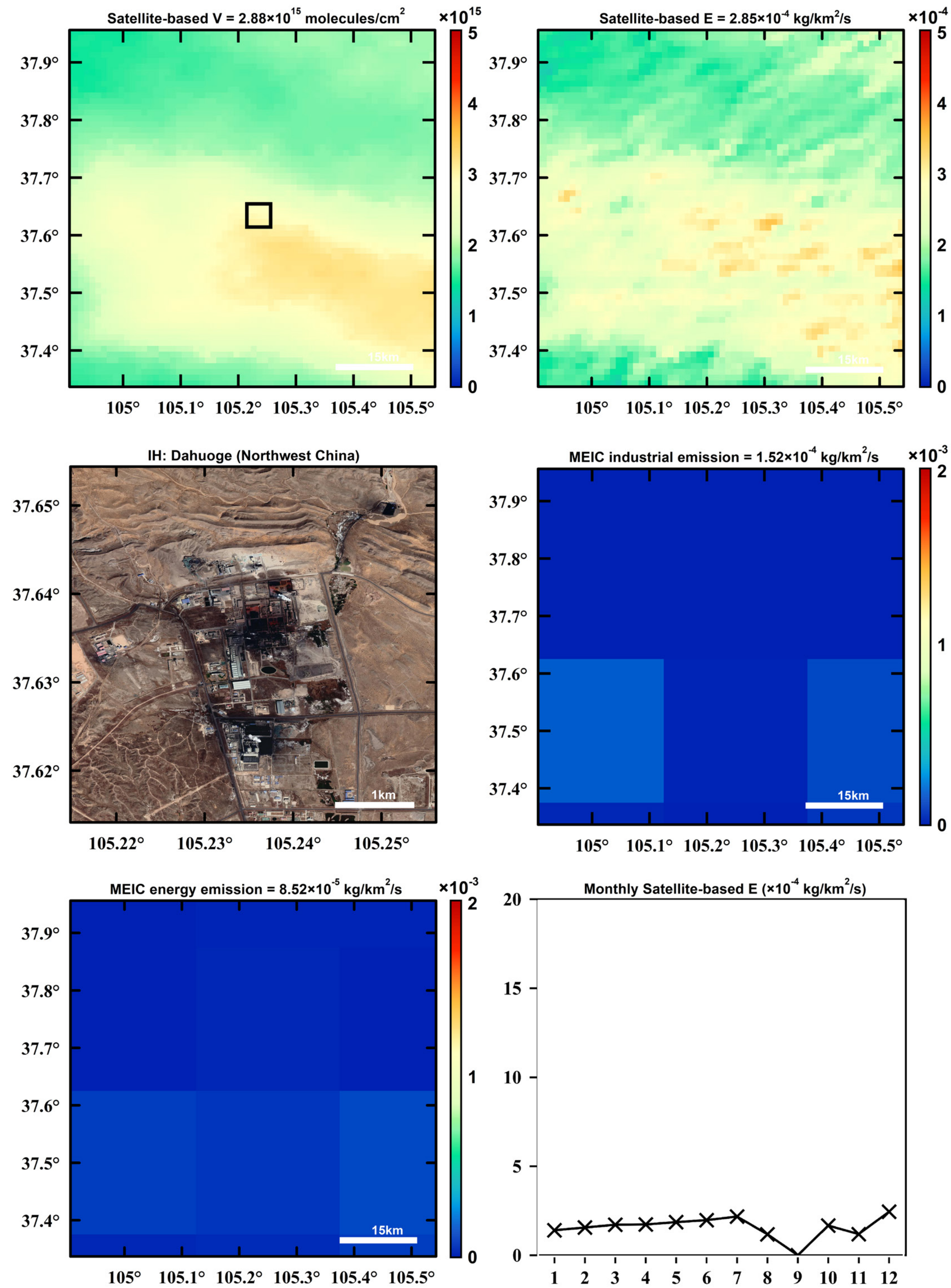

Fig. S7. The same as Fig. 2 but for different super-emitters. The representative super-emitters show stable monthly variations in the satellite-based NO_x emission fluxes **(Fig. S7c)**.

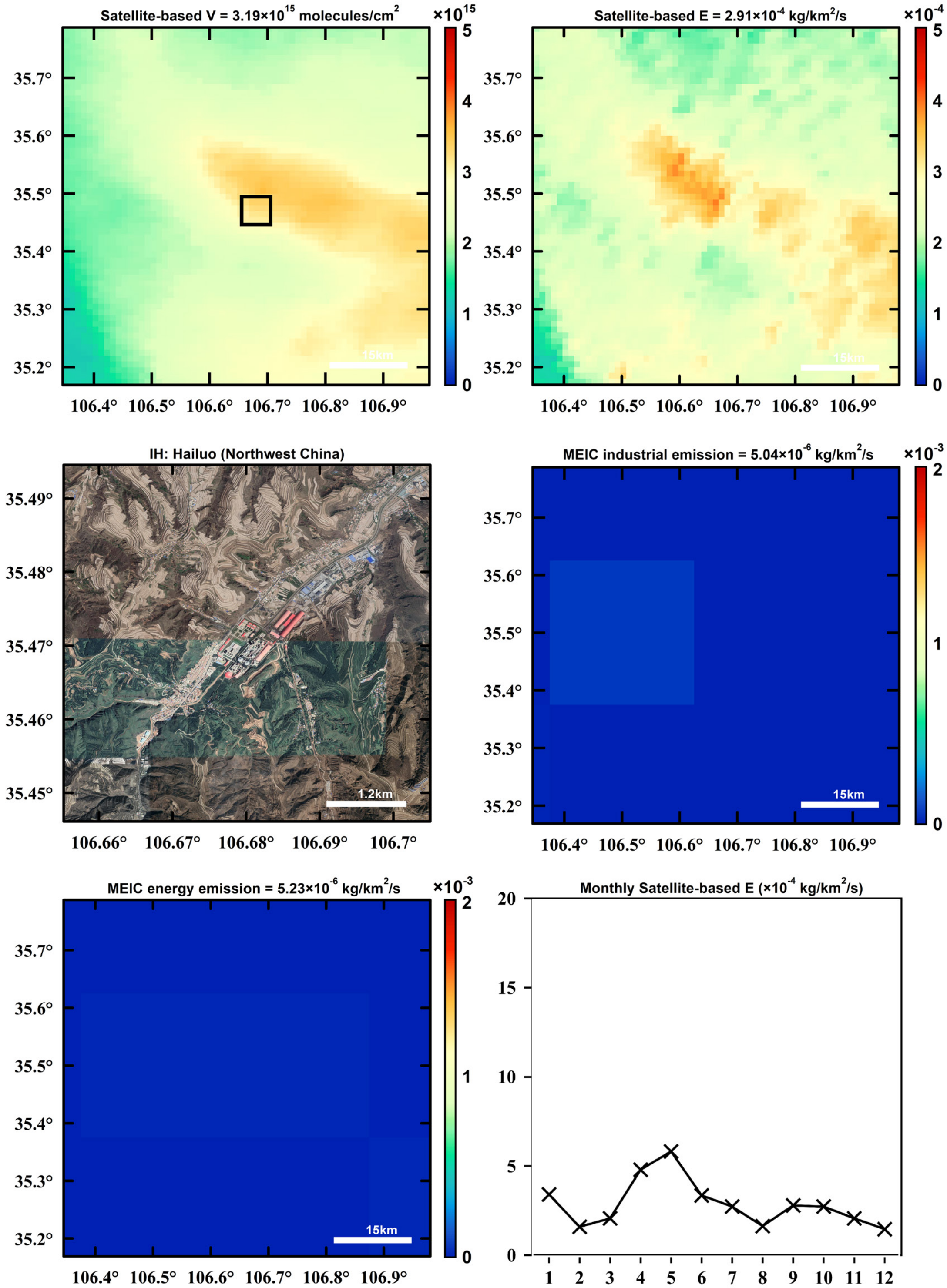

Fig. S7. The same as Fig. 2 but for different super-emitters. The representative super-emitters show stable monthly variations in the satellite-based NO_x emission fluxes **(Fig. S7d)**.

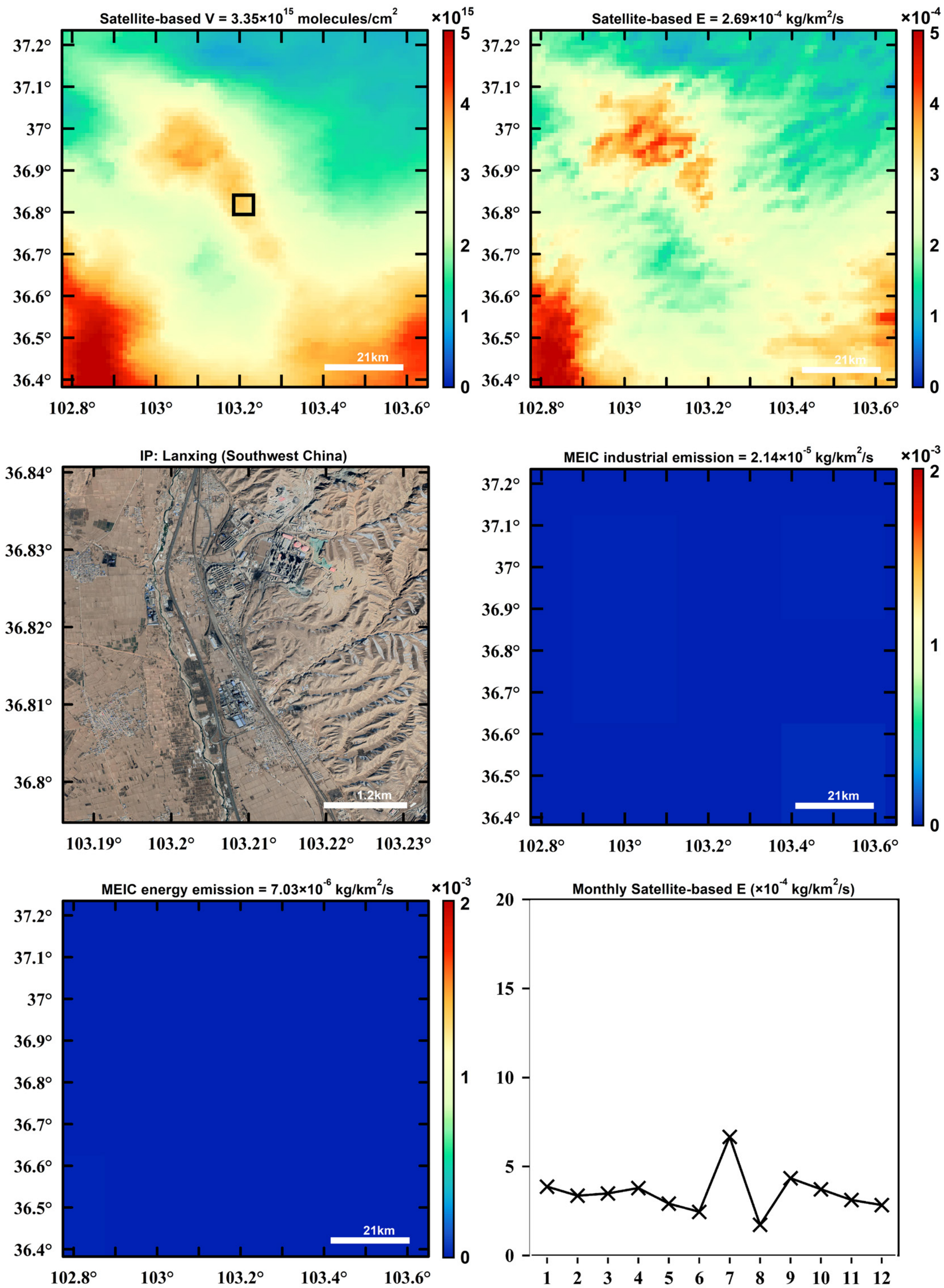

Fig. S7. The same as Fig. 2 but for different super-emitters. The representative super-emitters show stable monthly variations in the satellite-based NO_x emission fluxes **(Fig. S7e)**.

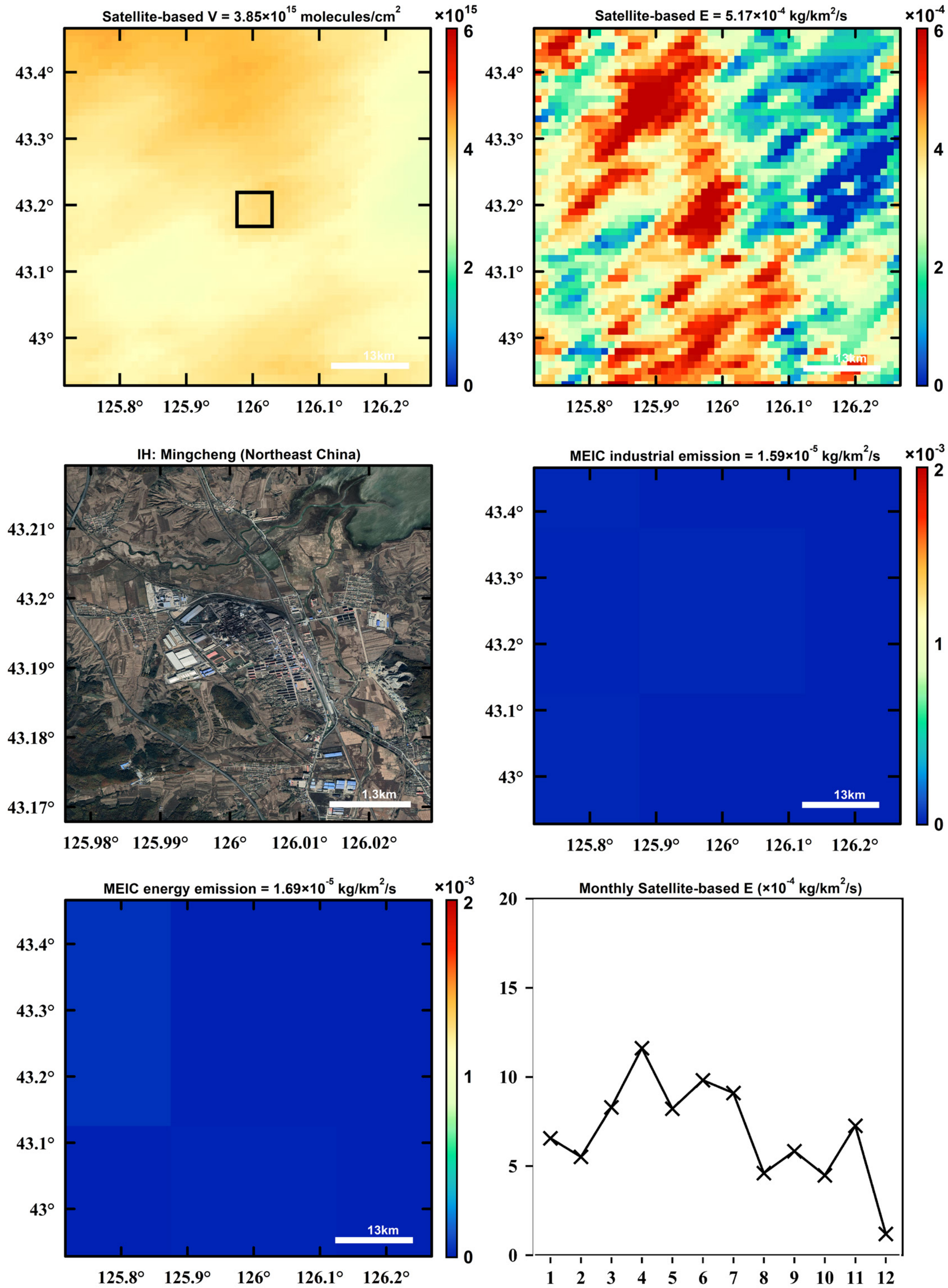

Fig. S7. The same as Fig. 2 but for different super-emitters. The representative super-emitters show stable monthly variations in the satellite-based NO_x emission fluxes **(Fig. S7f)**.

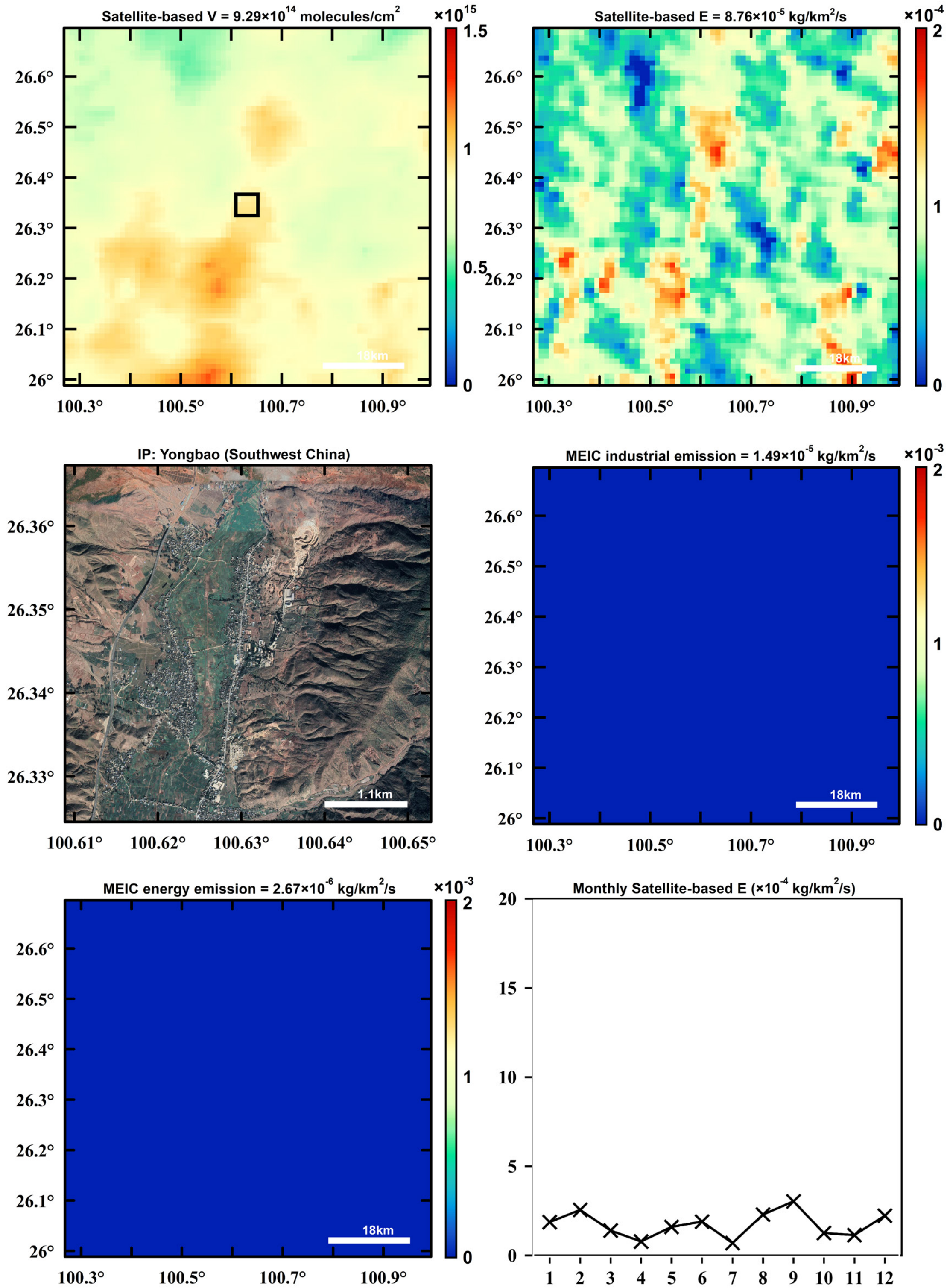

Fig. S7. The same as Fig. 2 but for different super-emitters. The representative super-emitters show stable monthly variations in the satellite-based NO_x emission fluxes **(Fig. S7g)**.

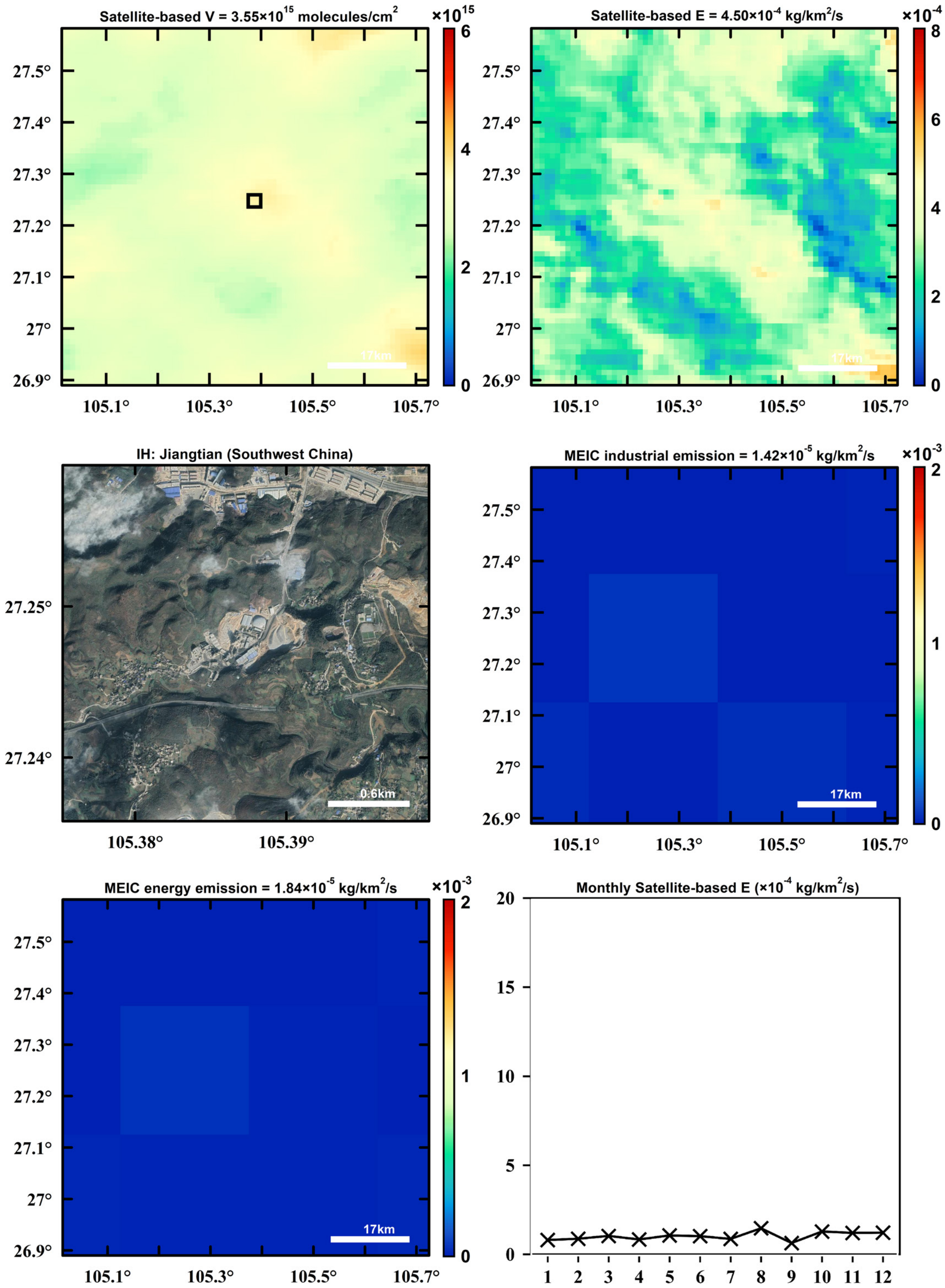

Fig. S7. The same as Fig. 2 but for different super-emitters. The representative super-emitters show stable monthly variations in the satellite-based NO_x emission fluxes **(Fig. S7h)**.

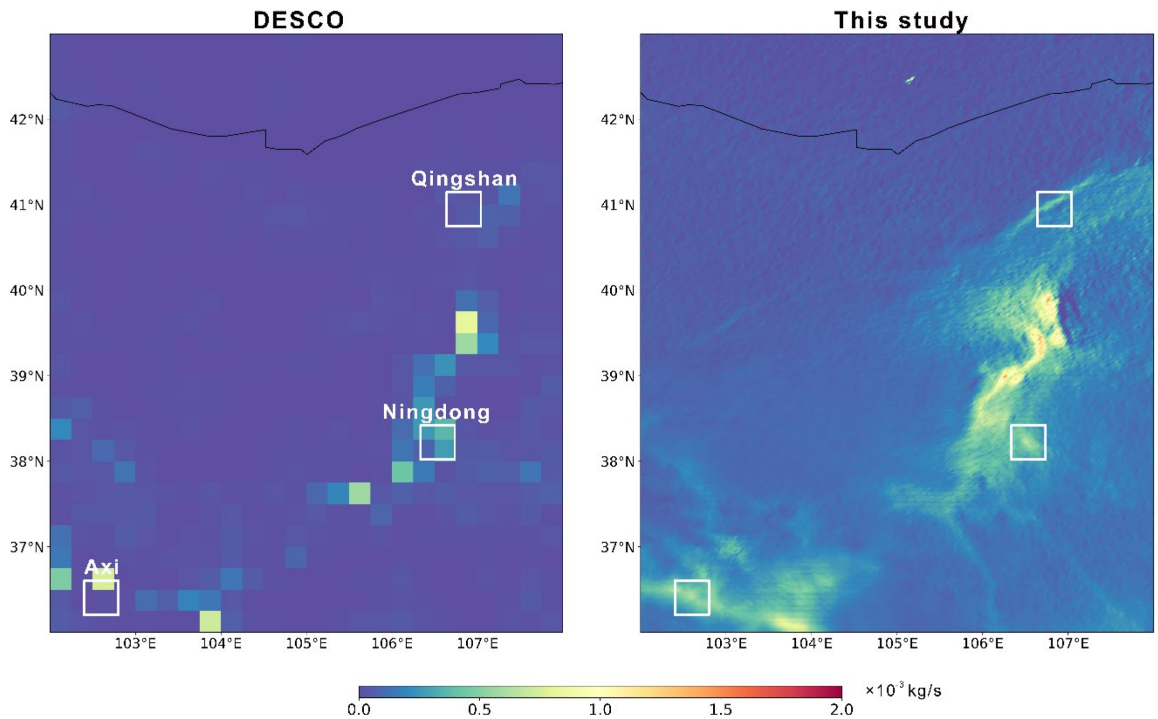

Fig. S8. Comparison of top-down NO_x emissions for two representative super-emitters in this study with those in a state-of-the-art emission inventory. The right panel presents our estimations on a 1×1 km^2 grid, while the left panel previous results using a distinct inverse algorithm (DESCO) on a $0.25° \times 0.25°$ grid. The substantial increase in spatial resolution allows the identification of three super-emitters, including Qingshan, Ningdong, and Axi, marked in the left panel.

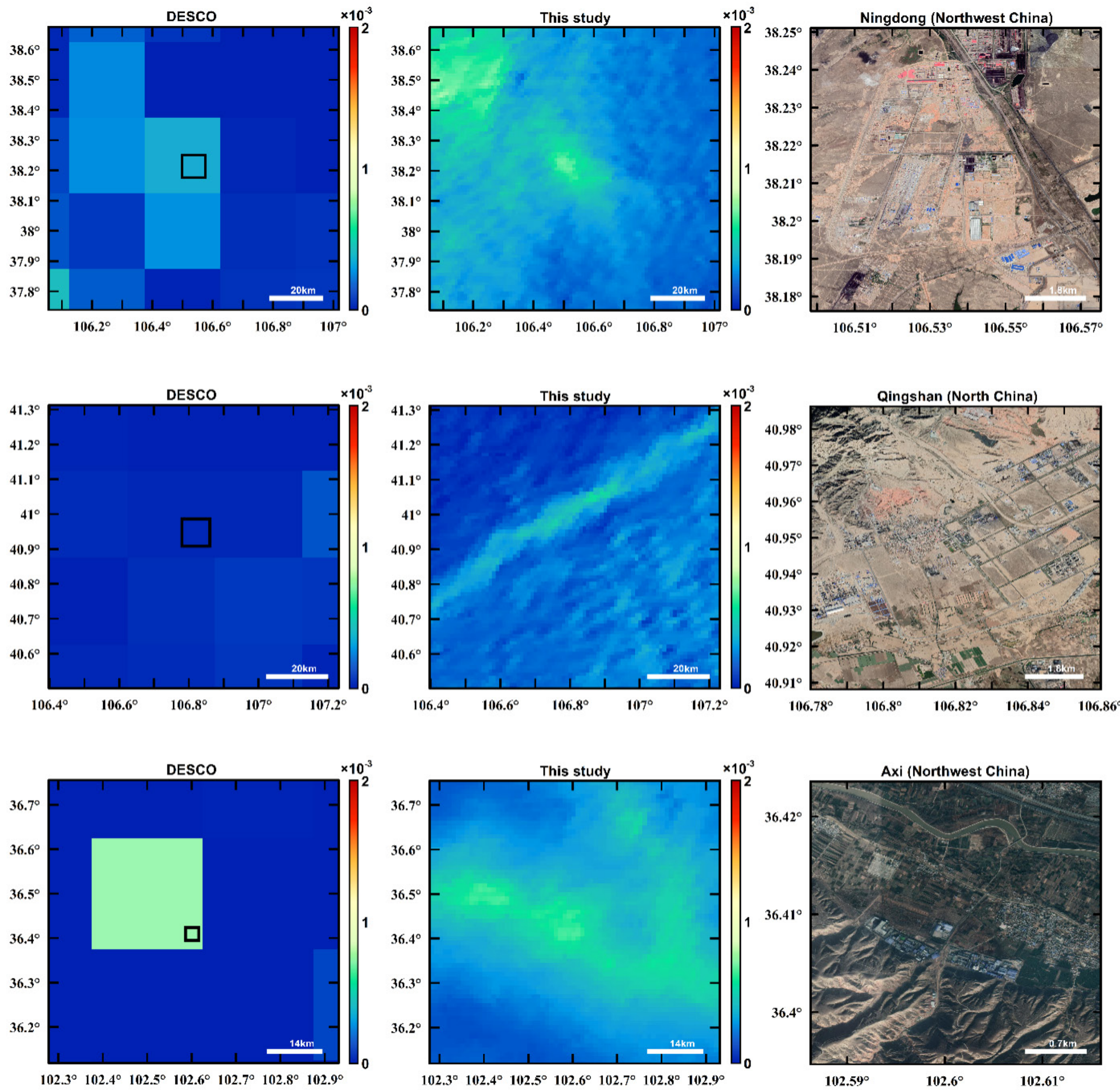

Fig. S9. The detailed information of the representative super-emitters in Fig. S8. The medium panel presents the enlarged view of our estimations on a 1 × 1 km^2 grid, while the left panel the enlarged view of previous results using a distinct inverse algorithm (DESCO) on a 0.25° × 0.25° grid. The substantial increase in spatial resolution allows the identification of three super-emitters, including Qingshan, Ningdong, and Axi, marked in the left panel.

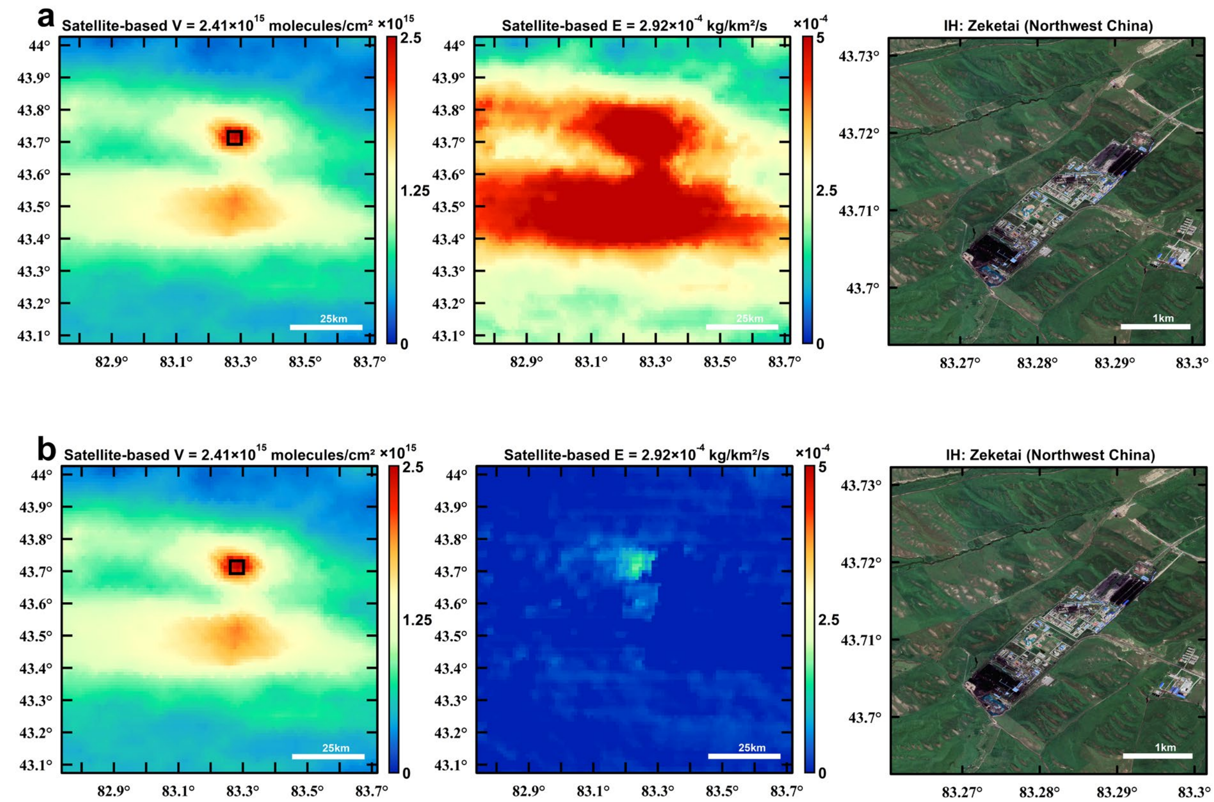

Fig. S10. The re-calculated NO_x emission fluxes for Zeketai in Fig. 2a. The NO_x lifetime in the top-down inverse model is adjusted to **(a)** 1 and **(b)** 24 hours.

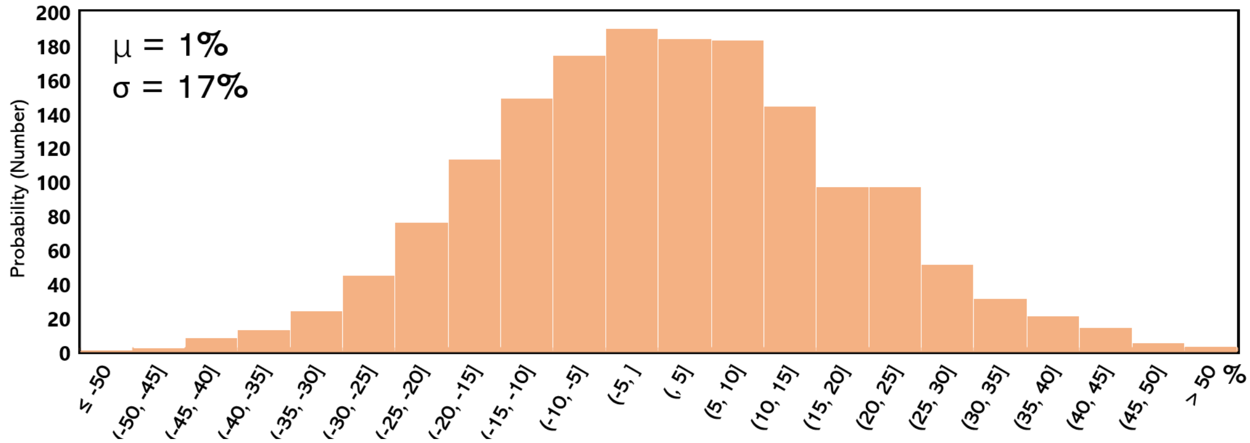

Fig. S11. Uncertainty analysis for vertical profiles. The relative differences (%) are calculated as the baseline data minus the test data, divided by the baseline data. We compared the satellite-based NO_x VCDs in this study (the baseline data) with those applied the MEICv1.2-driven (the base year was 2012) WRF-CMAQ model simulations (the test data).

Table S1. NO_x lifetime estimates reported in the literature.

Reference	Lifetime	Comment
Steffen Beirle et al., 2012[4]	4 ~ 8 hours	Daytime lifetimes are ~4 hours at low and mid-latitudes, but ~8 hours in wintertime for Moscow.
Steffen Beirle et al., 2019[7]	4 hours	The daytime lifetime is ~4 hours around Riyadh
Fei Liu et al., 2016[13]	3.8±1.0 hours	The mean lifetime is 3.8±1.0 hours with a range of 1.8 to 7.5 hours for the ozone season in the United States and China.
Hao Kong et al., 2019[14]	0.6 to 3.3 hours	The total lifetime varies from 0.6 to 3.3 hours for the summer months (June, July, and August) in the Yangtze River Delta.
Joshua L. Laughner et al., 2019[15]	1 ~ 6.5 hours	The absolute weekday lifetime is within a range of 1 ~ 6.5 hours for North American cities.